How hydroxyapatite governs surface Cu(II) and Fe(III) structuring: effects in the N_2O decomposition under highly oxidant atmosphere

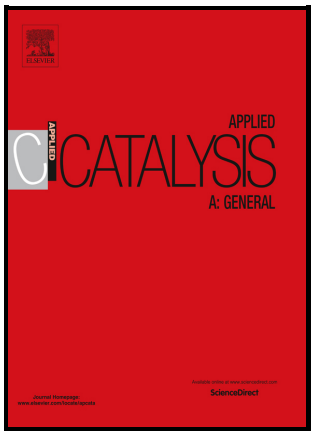

Melissa Greta Galloni, Sebastiano Campisi, Antonella Gervasini, Sara Morandi, Maela Manzoli

PII: S0926-860X(23)00081-9

DOI: https://doi.org/10.1016/j.apcata.2023.119101

Reference: APCATA119101

To appear in: *Applied Catalysis A, General*

Received date: 14 December 2022
Revised date: 15 February 2023
Accepted date: 16 February 2023

Please cite this article as: Melissa Greta Galloni, Sebastiano Campisi, Antonella Gervasini, Sara Morandi and Maela Manzoli, How hydroxyapatite governs surface Cu(II) and Fe(III) structuring: effects in the N_2O decomposition under highly oxidant atmosphere, *Applied Catalysis A, General,* (2022) doi:https://doi.org/10.1016/j.apcata.2023.119101

How hydroxyapatite governs surface Cu(II) and Fe(III) structuring: effects in the N_2O decomposition under highly oxidant atmosphere

Melissa Greta Galloni,[1] Sebastiano Campisi,[1*] Antonella Gervasini,[1*] Sara Morandi,[2] and Maela Manzoli [3]

[1] *Dipartimento di Chimica, Università degli Studi di Milano, via Camillo Golgi 19, 20133 Milano, Italy*

[2] *Dipartimento di Chimica, NIS - Centre for Nanostructured Interfaces and Surfaces, and INSTM Reference Centre, Università degli Studi di Torino, Via Pietro Giuria, 7, 10125 Torino, Italy*

[3] *Dipartimento di Scienza e Tecnologia del Farmaco, NIS - Centre for Nanostructured Interfaces and Surfaces and INSTM Reference Centre, Università degli Studi di Torino, via Pietro Giuria 9, 10125 Torino, Italy*

AUTHORS' INFORMATION

Corresponding Author
**E-mail: antonella.gervasini@unimi.it*
sebastiano.campisi@unimi.it

ORCID
Melissa Greta Galloni: 0000-0001-5446-5186
Sebastiano Campisi: 0000-0002-5496-7482
Antonella Gervasini: 0000-0001-6525-7948
Sara Morandi: 0000-0003-0577-7911
Maela Manzoli: 0000-0002-4427-7939

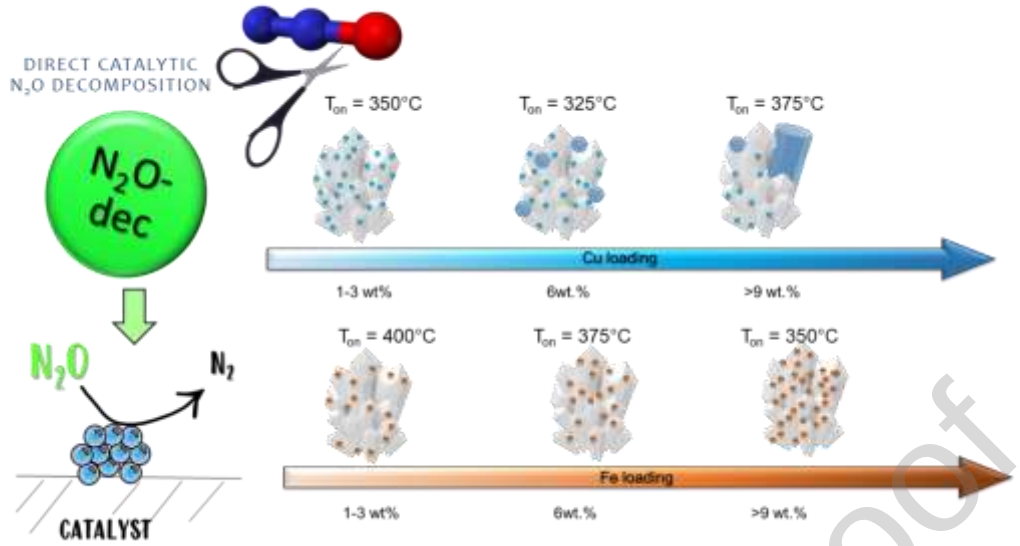

Abstract

In this work, we present copper- or iron-loaded hydroxyapatite samples as active catalysts in the direct N_2O decomposition reaction. Hydroxyapatite, functionalized with increasing amount of Cu(II) or Fe(III) species (from 3 to 9 wt.%), were characterized by P-XRD, UV-Vis-DRS, XPS, CO-adsorption followed by FT-IR, TEM-EDS, and tested in the N_2O decomposition. Stability tests (550°C, 72 h), reusability, resistance to sulfur (50 ppm) and to alkali (*ca.* 1 wt.% of K or Ba) completed the study of the catalyst performances.

Copper catalysts showed superior performances than iron counterparts. The structural evolution of the metal species with loading plays a critical role in the catalytic behavior. In the case of Fe-catalysts, a gradual Fe-coverage of HAP surface resulted in an increasing trend in the activity. Conversely, for Cu-catalysts, high activity and selectivity were associated with a moderate structuration of Cu(II) in the form of nanoparticles with size around 1.6 nm.

Key words*: waste derived material; copper; iron; surface characterization; catalyst stability; sulfur poison, alkali poison*

Introduction

Nowadays, a captivating challenge for environmental reactions is the rational design of efficient catalysts able to take on the new challenges of the economy and environmental sustainability of the processes. A catalytic structure needs to be performant, but, at the same time, should be easy to handle and manage, from its creation to the disposal. In this perspective, requirements of non-toxicity, biocompatibility, and bioavailability are thus strongly recommended for catalysts to use in environmental reactions.

In this field, hydroxyapatite (HAP, $Ca_{10}(PO_4)_6(OH)_2$), a bioavailable and biocompatible crystalline bioceramic material, has gained increasing interest due to its peculiar properties, such as thermal and chemical stability, structure flexibility, and highly functionalized surface able to allocate several metal ionic species [1–5]

Recently, copper- and iron-functionalized hydroxyapatite catalysts (Cu/HAP and Fe/HAP) have been revealed to be promising in some environmental reactions aimed at abating nitrogen-containing air pollutants, such as nitrogen oxides (NO_x), ammonia (NH_3), and nitrous oxide (N_2O) [6–9]. As concerns NO_x reduction (NH_3-SCR), on Fe/HAP catalysts NO_x started to be converted at higher temperatures and conversion was always lower than on Cu/HAP ones. Selectivity to N_2 was very high (> 95%) at any temperature up to maximum NO_x conversion; for higher temperatures, selectivity to N_2 decreased due to the N_2O formation from NH_3 over-oxidation. Similar comparative studies on Cu/HAP and Fe/HAP in N_2O decomposition reaction have not been presented in the literature.

Nitrous oxide, N_2O, is today classified as the third most harmful greenhouse species and the largest stratospheric ozone depleting substance because of its G*lobal Warming Potential* (GWP *ca*. 300 times that of CO_2 for a 100-year timescale) and long lifetime in the atmosphere (*ca.* 150 years) [10–

12]. In addition to natural emissions, the N_2O concentration has been continuously increasing due to several anthropogenic activities.

The current total anthropogenic N_2O emissions, which mainly derive from the by-products of fertilisation, biomass, and especially industrial chemical processes (*e.g.*, nitric and adipic acid production and stationary or mobile combustion plants), could be estimated to be *ca.* 5.3 Tg N_2O-N/year (>10^{12} grams of nitrous oxide in equivalent nitrogen units per year). Unfortunately, an increase by more than 80% between 2005 and 2050 is expected if no additional future mitigation efforts will occur [13]

In this perspective, the control of N_2O emissions represents a fundamental need to fulfil the current stringent legislative constraints [14,15].

Direct catalytic decomposition of N_2O into N_2 and O_2 inert gases (de-N_2O, Eq.1) is an exothermal spontaneous reaction, which currently represents the most attractive and viable after-treatment strategy for the N_2O abatement due to its simplicity, low cost, and low energy requirements [14,16–19]

$$N_2O \rightarrow N_2 + \tfrac{1}{2} O_2 \quad (\Delta_r H°_{298} = -82\ kJ\cdot mol^{-1} \text{ and } \Delta_r G°_{298} = -104\ kJ\cdot mol^{-1}) \qquad \text{Eq. (1)}$$

The key-point of de-N_2O reaction is to find an effective catalyst. Over the years, a wide variety of catalysts have been proposed, *i.e.*, noble metal supported catalysts,[20–22] metal oxides (bare oxides, mixed oxides, spinels and perovskites) [23–26], and metal exchanged zeolites [17,27–32]. In particular, some zeolitic structures (*e.g.*, ZSM-5, SSZ-13 and FER) exchanged with copper or iron species emerged for their promising catalytic performances in 400-700°C interval [17,29,33] .The topology, microporous structure, porosity, and composition of the zeolitic support assure high dispersion of the metal phase at the surface [29,34]. Nevertheless, although metal exchanged zeolites have been largely studied, they suffer from some not yet overcome practical drawbacks (*e.g.*, synthesis expensiveness, poor hydrothermal stability, and low sulphur and water resistance), that seriously limit their practical use [17,35,36]

With the purpose to find efficient catalytic systems characterized by environmental benign features, some hydroxyapatite-based catalysts functionalized with rhodium and cobalt species have been recently investigated for the de-N_2O reaction [37,38]. In particular, the former resulted to be highly efficient (total N_2O conversion at *ca*. 250°C), but, as expected, the practical application remains limited by the high cost of the active metal phase, whereas cobalt containing hydroxyapatite achieved total N_2O conversion at temperatures higher than 600°C [37].

Following this view, in this work, we explored the possibility to develop efficient eco-friendly catalysts by functionalizing the hydroxyapatite surface with Cu(II) and Fe(III) species in different amount (*ca.* 3-9 wt.%), according to a wet deposition procedure using nitrate salt precursors. The used hydroxyapatite material derived from NOVOSOL® process by Solvay [39]: the patented procedure consists in the treatment of inorganic exit products from sodium bicarbonate production. The resulting hydroxyapatite material represents a successful example of circular economy.

Texture, phase composition, coordination of the metal species, surface composition, and acidity of the Cu- and Fe-hydroxyapatite samples have been investigated through several characterization techniques (i.e., N_2 adsorption/desorption at -196°C, X-ray powder diffraction, UV-diffuse reflectance and X-ray photoelectron spectroscopies, NH_3-titrations, and CO adsorption followed by in situ FT-IR spectroscopy). To further assess the applicability of the new catalytic systems, besides catalytic tests, additional experiments of reusability, time-on-stream stability, as well as sulphur and alkali poisoning have been also investigated.

2. Experimental

2.1 Materials and catalyst preparation

Calcium hydroxyapatite (HAP) used in this work was kindly supplied from Solvay (Soda Ash & Derivatives, Belgium). Its preparation procedure, composition and properties were reported in

Ref.[41]. Precursors were inorganic salts that represent exit products from industrial production of bicarbonate.

Cu(II) and Fe(III) deposition on HAP was performed by wet deposition (D) procedure. Nitrate salts ($Cu(NO_3)_2 \cdot 3H_2O$, 99% from Carlo Erba and $Fe(NO_3)_3 \cdot 9H_2O$, 99% from Sigma Aldrich) were used as precursors of copper and iron species. In a typical preparation, about 6 g of dried HAP powder (previously dried at 120°C overnight) was added to 250 mL of metal nitrate solution with concentration in 0.01-0.02 M range for Cu-samples and of 0.013 M for Fe-samples, respectively, under vigorous magnetic stirring. The suspensions were maintained at 40°C for 24 h. After filtration, samples were recovered, thoroughly washed with hot water (40°C), dried at 120°C for 16 h, and eventually calcined at 500°C (at a controlled rate of 1°C/min) for 1 h under static air. For Fe-containing samples, the deposition procedure was applied twice to obtain the sample loaded with *ca.* 6 wt.% Fe, and three times to obtain the sample loaded with *ca.* 9 wt.% Fe [42].

The collected samples were denoted as CuX/HAP_D and FeX/HAP_D, where X is the metal loading (comprised between 3 and 9 wt.%). The loading of Cu and Fe on HAP was doubly checked by ion chromatography (Dionex DX-120 instrument, column IonPac CS5A; eluent: 50 mM oxalic acid/95 mM lithium hydroxide at pH 4.8, UV–vis detection, colorimetric indicator: 4-(2′-Pyridylazo)-resorcinol free acid in 3 M NH_4OH and 1 M acetic acid) on filtrate solutions derived from the deposition procedure and on digested solid samples (dissolution in HNO_3 5 M) and. Results were averaged and deviations were within +/– 0.05 wt.%.

The doping of $Cu6/HAP_D$ and $Fe9/HAP_D$ with K^+ and Ba^{2+} ionic species (dopant: Cu/Fe ~ 1:10, molar ratio) was performed by impregnation. For each preparation, about 1.3 g of powder sample (previously dried at 120°C overnight) was put in contact with 1 mL of a clear solution of potassium nitrate (0.12 M, KNO_3, 99% from Carlo Erba), or of barium nitrate (0.23 M, $Ba(NO_3)_2$, 99% from Sigma Aldrich) in 25 mL necked flask. The flask was connected to a Büchi GKR-50 rotary evaporator, the impregnation was performed under vacuum and rotation at 80°C. After the complete aqueous phase evaporation (*ca.* 2 h), the as-obtained samples were washed with *ca.* 5 mL of milliQ

water to remove the excess of nitrates and then dried at 120°C overnight. The K or Ba loading was checked by ion chromatography (Metrohm 761 compact IC with conductivity detector, column Metrosep C4, eluent H_3PO_4 5 mM) after acid digestion of an aliquot of solid sample. The as-obtained samples were labelled as Cu6/$HAP_{D,K}$, Cu6/$HAP_{D,Ba}$, Fe9/$HAP_{D,K}$ and Fe9/$HAP_{D,Ba}$.

2.2 Catalyst characterisation

N_2 adsorption/desorption isotherms were collected at -196°C by an automatic analyzer of surface area (Sorptomatic 1990 version instrument from Thermo Scientific Carlo Erba). Data were collected by MILES-200 program and processed by MILEADP Software.

Surface acid site titration of samples by NH_3-probe at 120°C was realised in dynamic experiments in a laboratory reaction line composed by a quartz reactor (in which *ca.* 0.2 g of catalyst, 45-60 mesh, was put) and an online FT-IR spectrophotometer (Bio- Rad with DTGS detector). Two series of NH_3 adsorption measurements were collected in succession to distinguish between total acid sites and strong acid sites, as described in the Supporting Information section.

X-ray powder diffraction (XRPD) patterns were collected by a Bruker D8 diffractometer (Cuα radiation at 0.154184 nm) equipped with a Ni filter and 1-D multistrip detector (LynxEye, 192 channels on 2.95°). Diffractograms were collected in 5°-65° (2θ) interval, step of 0.02° 2θ, time for step 96 s, total acquisition time in 34 min-2h range. An electronic discrimination (fluorescence conditions) in 0.18-0.25 V range was used for Fe/HAP_D diffractogram collection.

Diffuse Reflectance (UV-DR) spectra of samples in 200-2600 nm interval at room temperature were collected by a double beam UV–vis–NIR scanning spectrophotometer (Shimadzu UV-3600 plus, Japan) equipped with a diffuse reflectance accessory (integrating sphere from BIS-603).

X-Ray Photoelectron Spectroscopy (XPS) analyses were performed by an M-PROBE Surface Spectrometer equipped with an Al (Ka) source and a spot size from 0.15 mm to 1 mm in diameter and a 10 V applied voltage at a vacuum of 10^{-7} –10^{-8} Torr. Data were processed by ESCA Hawk Software: the normalized surface compositions of each species were computed by ruling out the

contribution of adventitious carbon (C–C at *ca.* 284.8 eV) while maintaning the components related to carbonate species.

Absorption IR spectra were collected at liquid nitrogen temperature (LNT, -196°C) with a Perkin-Elmer FT-IR system 2000 spectrophotometer equipped with a Hg-Cd-Te cryodetector, working in the range of wavenumbers 7200-580 cm^{-1} at a resolution of 2 cm^{-1} (60 scans). For IR analyses, the powder samples were pelletized in self-supporting disks (10 mg/cm^2) and placed in a home-made quartz IR cell allowing thermal treatments in vacuum or in controlled atmosphere and the recording of the spectra at liquid nitrogen temperature (LNT). Pellets were initially activated by thermal treatment at 400 °C in vacuum for 30 minutes and then in dry oxygen (40 mbar) for 30 minutes. After the treatment, samples were cooled down to RT in oxygen, outgassed and then made to interact with CO (Praxair, > 99.997%) at LNT. IR spectra were run at increasing CO pressure up to 30 mbar. In the figures, spectra are reported as difference spectra, where the subtrahend spectrum is that of the sample after the activation, before CO admission.

Transmission electron microscopy (TEM) and high resolution (HR)TEM images of $Cu3/HAP_D$ and $Cu6/HAP_D$ samples were obtained with a side entry Jeol 3010-UHR microscope operating at 300 kV equipped with a LaB_6 filament and fitted with an Oxford Inca Energy TEM 300 EDS X-ray analyzer by a Link ISIS 200 detector. Digital micrographs were acquired with an Ultrascan 1000 camera and processed with a Gatan digital micrograph.

Further experimental details on procedure and methods followed for the various characterization analyses are reported in Supporting Information paragraph.

2.3 Catalytic tests in de-N_2O reaction

Catalytic N_2O decomposition was investigated by a continuous reaction line, consisting of a set of mass flow controllers (Bronkhorst, Hi-Tech instruments), a tubular vertical electric oven (Eurotherm Controller-Programmer type 818), a glass tubular catalytic micro reactor (5 mm i.d.), and an online FT-IR spectrophotometer (Bio-Rad, DTGS detector) for qualitative and quantitative

determination of fed and vented gaseous species. The typical reaction conditions were: 150 ppm N_2O and 6000 ppm O_2 (N_2O/O_2=0.025); 300-800°C temperature range; contact time of *ca.* 0.12 s. These conditions could simulate N_2O emissions from industrial combustion processes (i.e. fluidised bed combustion, whose emissions contain ca. 50–200 ppm of N_2O and excess O_2) with the caveat that the reaction atmosphere did not contain water vapour, which, however, is often present in combustion process emissions [40]. N_2O conversion and selectivity to N_2 were computed according to equations reported in Table S.1.

Catalytic performances of two most promising catalysts of each series ($Cu6/HAP_D$ and $Fe9/HAP_D$) were examined in depth through reusability and time-on-stream stability tests. Reusability tests consisted in a first run carried out until the attainment of *ca.* 90% of N_2O conversion, and three successive courses of N_2O decomposition. Stability tests were performed at 550°C for 72 h on each catalyst. Moreover, on $Cu6/HAP_D$ and $Fe9/HAP_D$ samples, resistance to sulphur and alkali poisoning was investigated. Catalytic tests of N_2O decomposition from 300° to 800°C were performed in the presence of *ca.* 50 ppm of SO_2 in the gaseous stream. Doped samples ($Cu6/HAP_{D,K}$, $Cu6/HAP_{D,Ba}$, $Fe9/HAP_{D,K}$ and $Fe9/HAP_{D,Ba}$) were tests under typical reaction conditions.

The kinetic computations were performed by assuming a first-order rate equation for the reaction, according to the literature [43]. The rate dependence from the temperature has been evaluated by the Arrhenius plot and, accordingly, main activation parameters (apparent activation energy, E_{app}, and pre-exponential factor, A) were computed.

3. Results and discussion

3.1. Textural and compositional characterization of Cu/HAP and Fe/HAP catalysts

Eco-friendly catalytic systems based on HAP functionalized with copper or iron species were successfully prepared and studied in environmental reactions of air-quality protection (in particular NH_3-SCR and NH_3-SCO) in our previous works [6–9]. Herein, two catalyst series have been

prepared by functionalizing HAP with copper(II) and iron(III) ions in different amount (3-9% by weight), according to a wet-deposition procedure where a prolonged contact between the metal ions and HAP surface could favour a structuring of the metal species in the form of nanoaggregates. These tailored metal nanostructures have been discovered to possess high activity and selectivity in several gas-phase catalytic reactions [37,44–52]. Since, a controlled structuring of Fe-hydroxyapatite was harder to obtain than copper counterparts, a multi-step procedure of Fe deposition onto HAP was used to optimize the iron deposition with the final aim to prevent the uncontrolled phase aggregation.

Details on bulk and surface composition of all the samples, specific surface area, and total surface acidity are reported in Table 1.

In any case, metal concentration was close to that expected for both Cu- and Fe-samples, suggesting the quantitative immobilization of the metal species over HAP.

Texture of HAP and functionalized samples with metal ions species can be studied by adsorption and desorption isotherms of N_2, collected at liquid nitrogen temperature. Results already reported in the literature indicate moderate mesoporous materials with the possible presence of some micropores and surface area values of a few tens of square meters, depending on synthesis conditions and temperature treatment. HAP sample studied in this work had a surface area value of 75 $m^2 \cdot g^{-1}$ and presence of non-regular mesopores in size and shape. A decrease of surface area down to 53 $m^2 \cdot g^{-1}$ was observed after calcination at 500°C (Fig. S.1.). The addition of low amount of copper ($Cu3/HAP_D$) caused a very high increase of surface area (Table 1), likely due to surface reconstruction with presence of defective sites. Further addition of copper onto HAP ($Cu6/HAP_D$ and $Cu9/HAP_D$) gave rise to a trend inversion and surface area decreased as the amount of added copper increased (Table 1). This behaviour suggests a possible structuring of copper that has been studied in detail by microscopic investigation and XRPD and will be discussed here after below in this work. On the contrary, the addition of iron to HAP surface gave rise to the expected trend that the surface area values of the samples increased with increasing addition of iron, in the order:

$Fe3/HAP_D$, $Fe6/HAP_D$, and $Fe9/HAP_D$ (Table 1 and Fig. S.1.). In this case, the added Fe ions to HAP surface created additional exposed surface, likely due to FeO_x nanoaggregate formation, as already observed in similar samples through Mössbauer spectroscopy [6,7]. The comparative N_2 adsorption-desorption isotherms of bare and metal functionalized HAP samples are reported in Fig. S.1., in which $Cu6/HAP_D$ and $Fe9/HAP_D$ samples have been selected as representative samples.

Table 1. Main bulk and surface composition of Cu/HAP_D and Fe/HAP_D samples.

Code	Metal Loading[a]	Surface Area [b]	Total acid sites [c]	Me	Ca	P	(Ca+Me)/P
	%	$m_2 \cdot g^{-1}$	$\mu mol_{NH3(ads)} \cdot g^{-1}$			% [e]	
$Cu3/HAP_D$	2.98	84	187 (60%) [d]	2.16	17.1	13.8	1.40
$Cu6/HAP_D$	5.71	75	200 (76%)	1.49	15.0	11.7	1.41
$Cu9/HAP_D$	9.38	71	212 (67%)	2.30	15.8	13.4	1.35
$Fe3/HAP_D$	3.13	66	167 (41%)	1.58	13.0	11.4	1.28
$Fe6/HAP_D$	6.05	85	208 (56%)	3.63	12.0	12.9	1.21
$Fe9/HAP_D$	8.45	93	262 (73%)	3.61	9.72	11.9	1.12

[a] obtained on digested samples by ion chromatography; [b] surface area values of fresh and calcined (500°C) bare HAP were 75 $m^2 \cdot g^{-1}$ and 53 $m^2 \cdot g^{-1}$, respectively; [c] evaluated by I run of NH_3 titration on fresh samples; [d] percent of strong acid sites, determined by the difference between total and weak acid sites; [e] surface composition (in atomic percentage) obtained by XPS analyses.

Solid-gas acid-base titration of the samples by NH_3-probe was carried out to evaluate how Cu(II) and Fe(III) species, exposed at the surfaces, caused an increase of surface acidity in comparison with bare HAP due to their Lewis acid nature. The obtained titration profiles of all the samples are reported in Fig.s S.2. and S.3., whereas the results, (expressed as total and strong acid sites) are listed in Table 1. Bare HAP is characterized by an intrinsic acidity due to Ca^{2+} and PO-H surface groups, which act as Lewis and Brønsted acid sites, respectively; the number of total acid sites (*ca.* 130-140 $\mu mol_{NH3(ads)} \cdot g^{-1}$) was determined in our previous paper (Ref.[9]).

On the Cu/HAP samples, the addition of just 3 wt.% Cu on HAP caused a clear increase of the number of total acid sites (187 $\mu mol_{NH3(ads)}$ g^{-1}, Table 1), then, further Cu additions (6 wt.% and 9 wt.%) gave rise to samples with total number of acid sites of 200 and 212 $\mu mol_{NH3(ads)} \cdot g^{-1}$ (Cu6/HAP_D and Cu9/HAP_D, respectively, Table 1). In any case, the number of strong acid sites corresponded to *ca.* 60-76% of the total acid sites.

On the Fe/HAP samples, both total and strong acid sites increased with Fe-loading. In particular, a small addition of Fe on HAP (*ca.* 3 wt.%) gave rise to 167 $\mu mol_{NH3(ads)} \cdot g^{-1}$ as total acid sites, whose *ca.* 41% was strong sites (Table 1). Successive Fe-additions (*ca*. 6 wt.% and 9 wt.%) gave rise to samples with a number of total acid sites of 208 and 262 $\mu mol_{NH3(ads)} \cdot g^{-1}$ (Fe6/HAPD and Fe9/HAP_D, respectively, Table 1). of which *ca.* 56% and 73% corresponded to strong acid sites. The observed increase in the number of strong acid sites in the more Fe-loaded samples probably reflects surfaces that are increasingly covered with iron (as more Fe is added to the HAP surface), the iron thus covers the acidic sites of HAP that are of lower acidity.

The surface composition of all samples (Table 1, in atomic %) was determined by XPS analysis. Once again, the Cu and Fe surface atomic concentrations on the Cu/HAP and Fe/HAP samples followed a different trend. The surfaces of Fe3/HAP_D, Fe6/HAP_D, and Fe9/HAP_D became regularly enriched with Fe as the amount of Fe added increased, as expected. On the contrary, an unexpected situation involved copper: subsequent additions of Cu to the surface of HAP were not accompanied by a regular increase of Cu surface concentration.

As regards the presence of Ca on the surface of the samples (Table 1), it followed a trend parallel to that already described for the surface concentrations of Cu and Fe. The Ca concentration at the surface regularly decreased as the amount of Fe added to HAP increased, whereas absence of a regular trend for surface Ca was observed on the three Cu/HAP samples.

The last column of Table 1 reports the values of the (Ca+Me)/P surface ratio that should remain almost constant if Cu or Fe added to the HAP had exchanged with the Ca sites at the surface. For both Cu and Fe, a clear trend of decrease of the (Ca+Me)/P ratio was observed with the increase of the added amount of Cu and Fe, with a more regular decrease in the case of Cu. It can therefore be deduced that, for copper, an ion exchange (Ca^{2+}:Cu^{2+}) could take place without perturbing the electroneutrality of the HAP crystalline unit. However, the XPS experimental evidence (Table 1) indicates that the Cu entering the HAP surface did not compensate for the outgoing Ca (that is, (Cu+Ca)/P ratio decreased as the amount of total Cu on the surface increased). Likely, a surface reconstruction with also presence of copper ions in defectual/interstitial positions of HAP could occur, as already assumed from the modification of morphology observed on the Cu/HAP samples. A not too much dissimilar situation occurred in the case of Fe, in which the exit of a Ca ion for each Fe ion entering the surface is not expected, due to a problem of electroneutrality of the crystalline unit. In this case, the incoming Fe cannot compensate for all the outgoing Ca and the (Fe+Ca)/P ratio is destined to decrease as the Fe added to the HAP surface increases.

Summarizing, the metal functionalization of the HAP surface is a complex phenomenon and differs with the nature and properties of the metal ions; the charge of the ion and metal ion tendency to accommodate in interstitial positions govern the phenomenon with consequences on the amount of metal concentration present at the HAP surface.

3.2. Activity in N_2O decomposition

Catalytic performances in the de-N_2O reaction of all samples were evaluated by continuously feeding ca. 150 ppm of N_2O and 6,000 ppm of O_2 under fixed GHSV and variable temperature.

Although the catalysts were calcined at 500°C, in the first catalytic screening, a wide temperature range, up to 800°C, was selected with the sole scope to check the ability of the catalysts to achieve 100% conversion. In fact, it is known that the studied reaction requires high temperature due to high stability of the N_2O molecule.

Figure 1 reports the obtained catalytic results as profiles of N_2O conversion along with temperature for Cu- and Fe-samples (Fig. 1a and Fig. 1b, respectively), compared with that of bare HAP (dotted black lines). In the figure, filled and empty markers indicated N_2O conversion values up to or above 550°C, respectively.

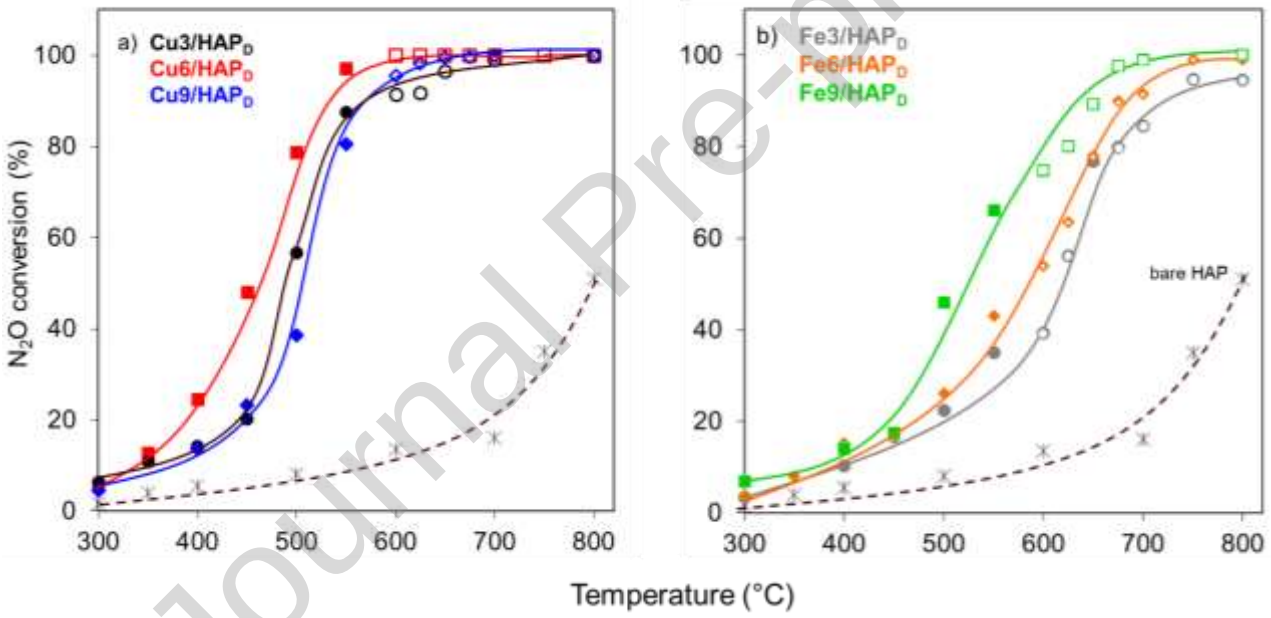

Figure 1. De-N_2O catalytic activity results: profiles of N_2O conversion (%) as a function of temperature (°C) over Cu/HAP$_D$, and Fe/HAP$_D$ samples (a and b panels, respectively), compared with that of bare HAP (dotted black line). Reaction conditions: [N_2O] =150 ppm, [O_2] = 6,000 ppm, contact time= 0.12 s. Filled and empty markers indicates N_2O conversion values collected up to and above 550°C, respectively.

Negligible catalytic activity was detected on bare HAP that started to be active at ca. 600°C and reached only 50% N_2O conversion at 800°C. Interestingly, the copper and iron functionalization of HAP imparted remarkable catalytic activity to surfaces. The onset temperature (temperature at

which at least 10% N_2O conversion was attained) was in 350-400°C range for all the samples. Sigmoidal *S-curves* then described the conversion increase along with the temperature. The rise's steepness of the curves varied depending on the metal species and metal loading. In general, the N_2O conversion rapidly increased over Cu-catalysts while Fe-catalyst showed a more gradual increase of N_2O conversion with the temperature. It is noteworthy that conversion higher than 90% on the best Cu-catalyst (Cu6/HAP) and higher than 70% on the best Fe/HAP were obtained at temperature close to the calcination temperature.

Regarding Cu-samples, an unexpected trend correlated the catalytic activity with Cu-loading: $Cu6/HAP_D$ emerged as the most active sample because it reached 50% N_2O conversion (T_{50}) at *ca.* 460°C and T_{99} at *ca.* 550°C. On the other hand, $Cu3/HAP_D$ and $Cu9/HAP_D$ samples resulted to be less active (T_{50} values of *ca.* 490 and 510°C, respectively) with the attainment of 99% N_2O conversion at only 650°C (T_{99}) on the sample with the highest Cu content ($Cu9/HAP_D$).

Differently, the catalytic activity of Fe-samples increased more regularly with the Fe-loading. The T_{50} trend was in the order: $Fe9/HAP_D$ (525°C) < $Fe6/HAP_D$ (600°C) < $Fe3/HAP_D$ (625°C).

Interestingly, no undesired by-products (e.g., NO, NO_2, N_2O_4 and N_2O_5) were observed by online FT-IR analysis of the gaseous effluents in the whole explored temperature range. In addition, the absence of N-element in XPS analyses on the used catalysts (see below), allowed to rule out the possible formation and precipitation of N-containing species on the catalyst surface. These observations confirmed that the catalytic N_2O decomposition reaction proceeded with 100% selectivity towards N_2 formation, without any parallel/consecutive competitive oxidation reactions that could be expected in the presence of oxygen in the reaction mixture, in particular at the highest attained temperatures.

When compared to relevant literature examples (Table S.2.), the observed T_{50} values are in line with those reported for different Cu- and Fe-containing catalysts. However, a reliable comparison is not always straightforward, due to the different adopted conditions.

The catalytic results and the observed trends require a critical rationalization through a targeted characterization, to investigate the nature, structure, and aggregation of copper and iron species at the surface of HAP and their relationships with the catalytic activity.

3.3. Structural, morphological and spectroscopic characterization of Cu/HAP and Fe/HAP catalysts

Figure 2 reports the collected X-ray powder diffraction (XRPD) patterns of the studied copper and iron samples. All of them revealed the typical reflection patterns of the crystalline HAP (JCPDS: 00-09-0432), regardless of the nature of metal and loading, indicating the maintenance of the HAP crystalline phase for all the samples, even in the case of the presence of a high metal loading.

No further peaks related to copper or iron crystal phases were identified, except in the case of the $Cu9/HAP_D$ diffractogram, in which peaks related to the presence of libethenite ($Cu_2(OH)(PO_4)$, JCPDS 01-083-2264) could be also detected.

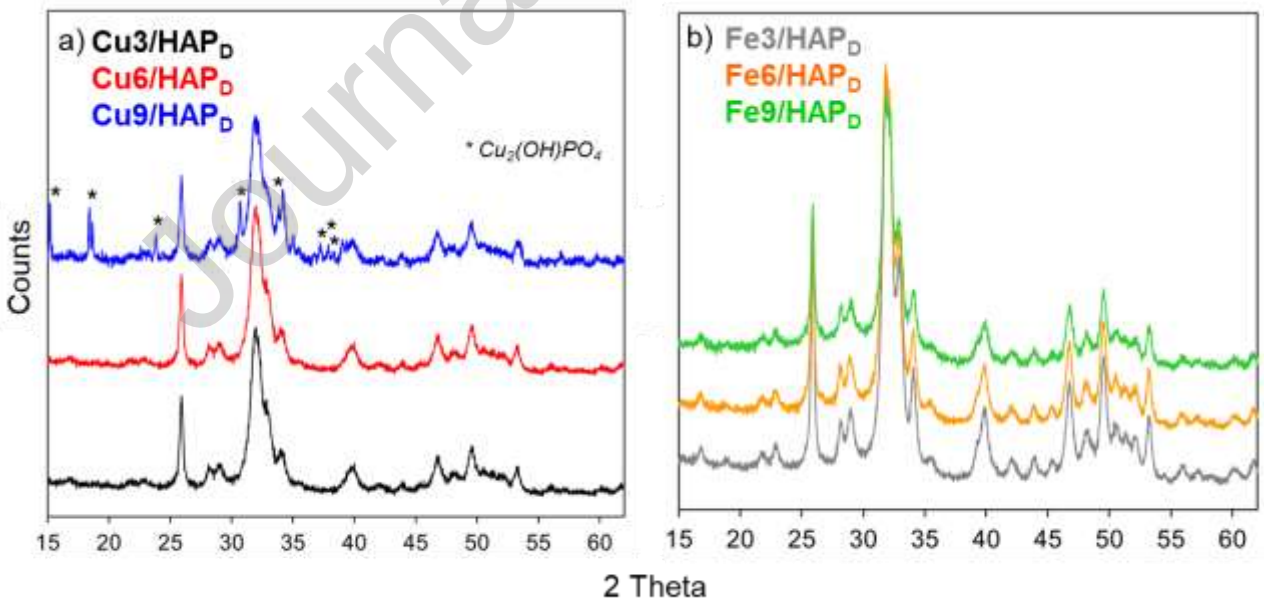

Figure 2. XRPD patterns of HAP (JCPDS 00-09-0432) of Cu/HAP_D and Fe/HAP_D samples (a and b panels, respectively). In panel a) the main reference patterns of libethenite ($Cu_2(OH)(PO_4)$, JCPDS 01-083-2264) are also reported.

Moreover, in all the diffractograms a decrease of the overall intensity was found as the metal loading increased, thus indicating a partial sample amorphization. These experimental evidences have allowed us to formulate some first hypotheses on the structure of copper and iron at the surface of HAP. Concerning Cu/HAP, an increase in the amount of copper at the surface of the samples led to the formation of a new crystalline copper phase which was clearly detected in the sample with the highest Cu loading ($Cu9/HAP_D$). As regards the iron catalysts, the presence of crystalline iron aggregates or new phases containing Fe-phosphate or Fe-oxide could be excluded, even in the sample with the highest metal loading ($Fe9/HAP_D$). On the other hand, it would also be possible the situation in which the copper and iron species could be present as amorphous phases or in the form of small oxidic or phosphatic aggregates, not detectable by XRPD because below the limit of detection.

UV-Vis DR spectra were collected to investigate the presence of aggregates of metallic species formed on the Cu/HAP and Fe/HAP surfaces: the obtained spectra are reported in Fig. 3 limited to 200-1800 nm and 200-800 nm ranges for Cu- and Fe- samples, respectively. The collected spectra were quite complex, and so deconvolution in sub-bands was necessary to discriminate among the different contributions. Different absorption bands were ascribable to ligand-to-metal charge transfer (*CT*) excitations from the O(2p) non-bonding valence bands to metal ligand field orbitals ($O^{2-} \rightarrow Cu^{2+}$ or $O^{2-} \rightarrow Fe^{3+}$) or to *d-d* (ligand field) transitions.

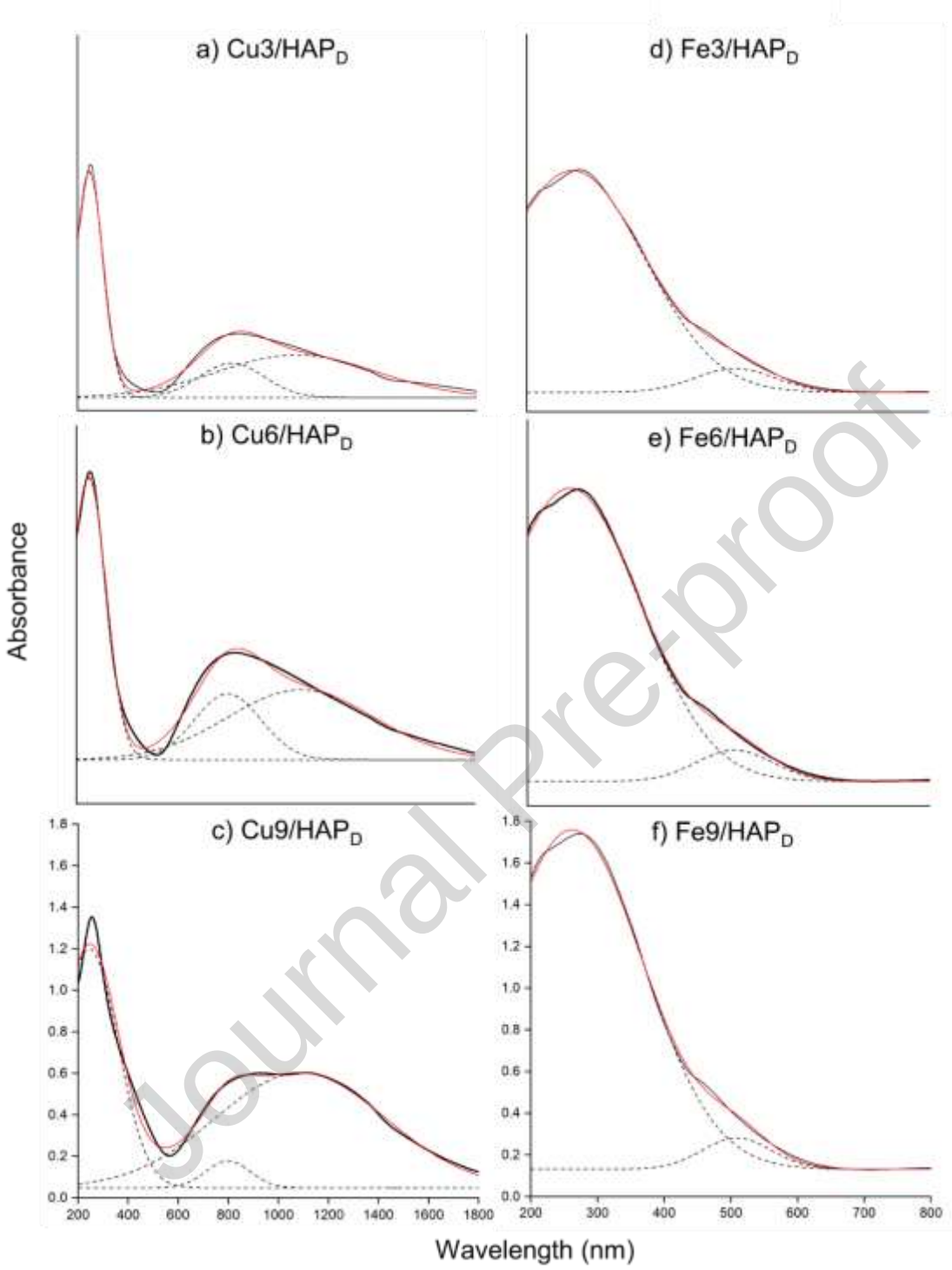

Figure 3. UV-vis DR spectra (black lines) of Cu/HAP$_D$ and Fe/HAP$_D$ samples (a-c and d-f, respectively). Decomposed curves (dotted black lines) and total calculated curves (red lines) are also reported.

All the spectra were characterized by a band of low intensity at *ca.* 200 nm (Figure S.4.), attributable to two different $O^{2-} \rightarrow Ca^{2+}$ *CT* arising from the two Ca^{2+} sites of the HAP framework, columnar Ca(I) and screw Ca(II) sites [1]). Two main absorption bands characterized the spectra of

the Cu/HAP samples: *i)* intense *CT* bands in 200-300 nm, range ascribable to isolated Cu^{2+} species and *ii) d-d* bands in 600-1200 nm interval, related to the presence of Cu^{2+} species in different coordinative environments. The contribution at higher wavelength clearly grew with the Cu-concentration in the samples, in the order: $Cu3/HAP_D$, $Cu6/HAP_D$, and $Cu9/HAP_D$. This band could be attributed to Cu^{2+} in the libethenite phase, which grew as the concentration of copper on the HAP increased, in accordance with what was observed by the XRPD patterns.

Also, the UV-vis DR spectra of Fe/HAP possessed two main features: *i)* intense *CT* bands in 200-300 nm range, related to isolated Fe^{3+} species and *ii)* intermediate bands in 460-500 nm window, corresponding to *d-d* or *CT* transitions of oligomeric Fe-O-Fe species [53,54]. In this case, it was not possible to detect any significant difference between the spectra of the three Fe-samples. This confirmed what has already been observed by the XRPD patterns of the Fe/HAP samples, no formation of large oxide/phosphate aggregates occurred, also on the highest concentrated sample.

The complex Cu- and Fe-speciation at the surface of the Cu/HAP and Fe/HAP samples were studied by High Resolution (HR) spectra of the primary XPS 2p regions of Cu- and Fe (Fig. 4). Regarding Cu-samples, the HR Cu-spectra, limited to 920-970 eV region (Figure 4, a-c) showed different contributions, which were solved by decomposing each detected peak in sub-bands. In general, in all the spectra, two main components in the 931.3-935.2 eV and 951.2-955.7 eV ranges were identified as Cu $2p_{3/2}$ and Cu $2p_{1/2}$ contributions. Each component was deconvoluted in two sub-curves with a spin-orbit splitting value (ΔE) of about 19.9-20 eV, typical of copper species. In particular, in the XP spectrum of $Cu3/HAP_D$, the Cu $2p_{3/2}$ main sub-band was centred at 931.3 eV and the second-one at 932.7 eV; they are typical of Cu(I) species, whose presence was confirmed by CO adsorption followed by FT-IR spectroscopy as well, as will be discussed in the bottom of this work. A different situation was observed in the XP spectra of the $Cu6/HAP_D$ and $Cu9/HAP_D$ samples. In both spectra, Cu $2p_{3/2}$ and $2p_{1/2}$ components were identified along with weak satellite peaks. In any case, these components were centred at higher BE values than those observed for $Cu3/HAP_D$. In particular, the Cu $2p_{3/2}$ sub-bands were centred at 933.2 and 935.0 eV and 933.4 and

935.2 eV with satellite contributions at 942.6 and 962.8 eV and 943.2 and 962.8 eV for Cu6/HAP_D and Cu9/HAP_D samples, respectively. According to the literature [55], these contributions could be associated to the presence of Cu(II) species surrounded by carbonate species as well as to Cu(II)-oxide species.

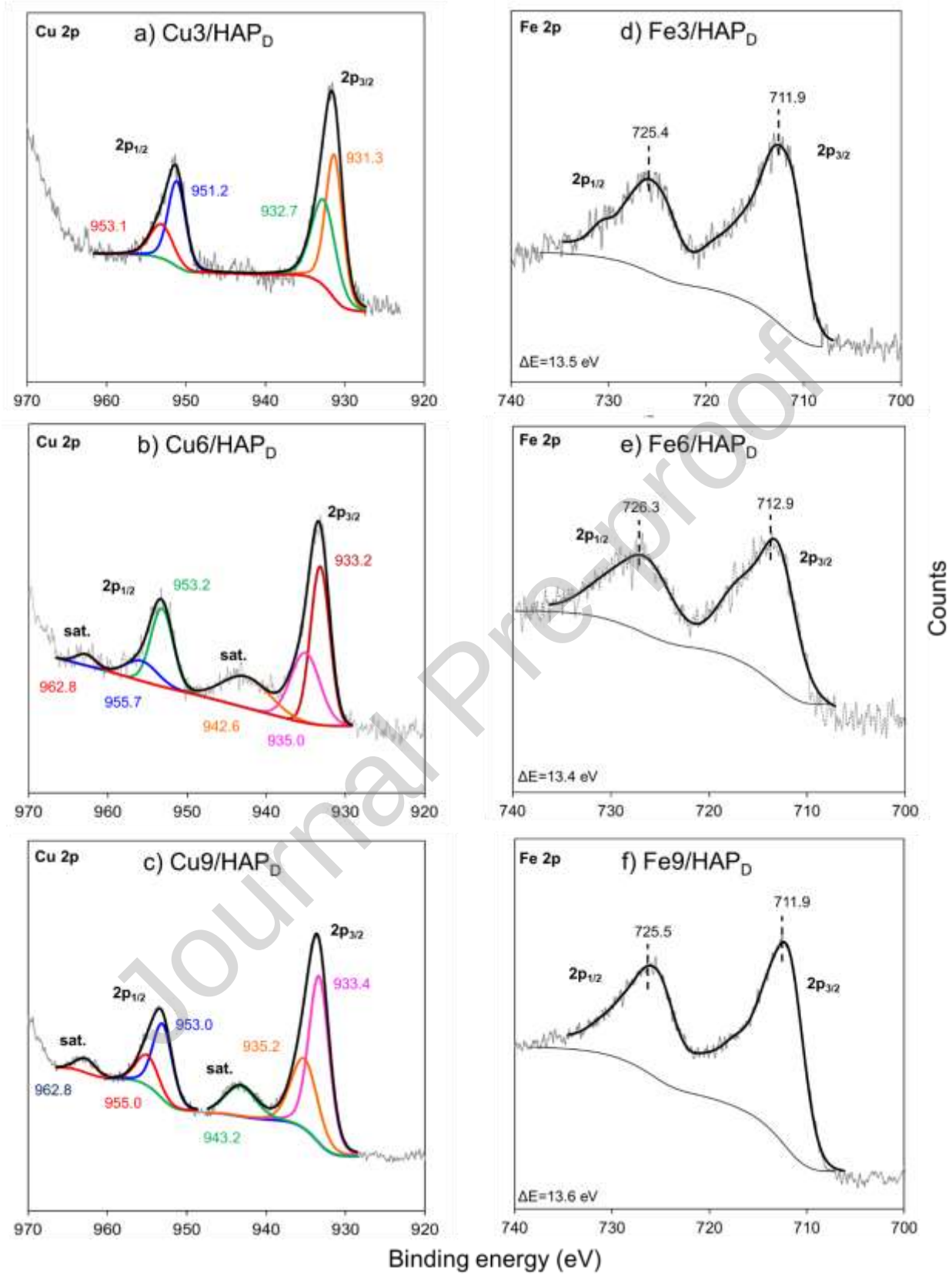

Figure 4. High-Resolution (HR) XP spectra of Cu/HAP$_D$ (a-c, left: Cu 2p) and Fe/HAP$_D$ (d-f, right: Fe 2p) samples. For Cu-HR spectra the related decompositions in sub-bands (red, blue, green, orange, pink, brown lines) and the resulting fitted spectra (black lines) are also represented, whereas for Fe-HR spectra binding energy values of Cu 2p$_{1/2}$ and 2p$_{3/2}$ peaks are reported.

Regarding Fe-samples, the HR XP spectra in 700-740 eV region (Fig. 4) were characterized by an evident high complexity due to the multiplet splitting and satellite features that could be discriminated. However, as the decomposition of Fe 2p spectra is debated in literature, the collected spectra were fitted with the only aim to identify the centres of the Fe $2p_{3/2}$ and $2p_{1/2}$ peaks. The determined values of the Fe $2p_{3/2}$ and $2p_{1/2}$ peak centres for the Fe3/HAP_D, Fe6/HAP_D, and Fe9/HAP_D samples are very similar to each other (Fig. 4). This evidence clearly confirmed what had already emerged from the XRPD and UV-V-DRS survey; the addition of iron to the HAP surface caused an increase in the surface concentration of Fe without the formation of segregated phases or large FeO_x aggregates.

Following the characterization study of the Cu/HAP_D and Fe/HAP_D samples reported above, a clear picture emerges for the Fe/HAP_D samples, whereas that for the Cu/HAP_D samples has not been completely clarified by the studies carried out. On these latter samples, some unclear points must be clarified regarding the structuring and surfacing of the copper centers in order to rationalize the de-N_2O activity observed on Cu catalysts (Fig. 1). In particular, clarity must be made on the inverse trend relative to Cu3/HAP_D and Cu6/HAP_D for the de-N_2O activity and surface concentration of Cu.

In order to investigate and clarify the nature and availability of the cationic surface sites on the two Cu3/HAP_D and Cu6/HAP_D samples (and also for comparison, on bare HAP), CO adsorption followed by FT-IR spectroscopy was performed. The HAP spectra (Figure 5, panel a) were characterized by a broad band at 2166 cm^{-1} related to CO bonded to Ca^{2+} sites [56]. The band appeared at 2180 cm^{-1} at low pressure (inset of Figure 5a) and shifted towards lower wavenumbers upon increasing CO coverage: this shift, called *chemical effect*, reflects a change in the bonding of CO as a function of coverage [57]. The observed red shift with coverage is characteristic when the coordination of CO to the site is accomplished by a σ bond, as in the case of Ca^{2+} cations. The band related to carbonyls of Ca^{2+} appeared at 2156 cm^{-1} (2170-2173 cm^{-1} at low CO coverage) in the

spectra of Cu3/HAP_D and Cu6/HAP_D (Figure 5 panel b and c, respectively). It is evident an influence of Cu on the stretching mode of Ca^{2+} carbonyls, whose band was shifted of 10 cm^{-1} towards lower wavenumbers with respect to that of bare HAP. However, the high coverage frequency (2156 cm^{-1}) is also influenced by the presence of Cu^{2+} carbonyls: as a matter of fact, bands related to CO bonded to Cu^{2+} and Cu^{+} sites were observed at 2160 and 2120 cm^{-1}, respectively[58] and references therein. These bands were particularly evident in the low-pressure spectra reported in the insets of Figure 5b and 5c. Carbonyls of Cu^{+} are the most stable and, as a consequence, they formed first (band at 2120 cm^{-1}). Upon increasing CO pressure, the band related to CO on Cu^{2+} (2160 cm^{-1}) appeared. This band became a shoulder of the band related to Ca^{2+}-CO species at 2156 cm^{-1} starting from 0.2 mbar of CO pressure (magenta trace). The intensities of Cu^{2+}-CO and Cu^{+}-CO bands were higher for Cu3/HAP_D than for Cu6/HAP_D catalyst, putting in evidence a lower availability of Cu-cations on the Cu6/HAP_D surface than on Cu3/HAP_D one, in agreement with the surface composition obtained by XPS analyses.

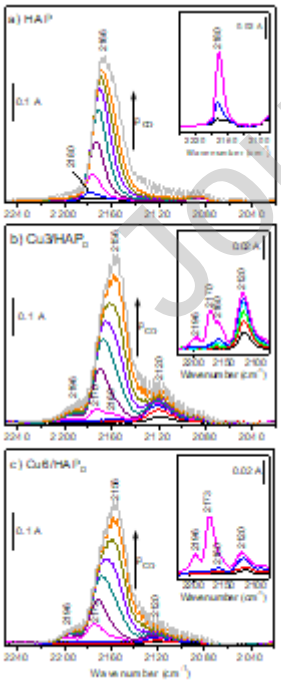

Figure 5 FT-IR spectra of CO adsorbed at LNT and increasing pressure up to 30 mbar on HAP (a), Cu3/HAP_D (b) and Cu6/HAP_D (c). Insets: zoom on the spectra recorded at low CO pressures (up to 0.2 mbar).

Finally, another band, not present for the bare HAP, was well evident at 2196 cm^{-1} for Cu3/HAP_D and Cu6/HAP_D catalysts. The same frequency is reported in literature for CO bonded to Ca^{2+} exchanged in zeolites [58,59] and references therein. Indeed, it is well known that cations in zeolite matrix are usually characterized by a low coordination number. This coordinative unsaturation is reflected into a stronger Ca^{2+} bond with CO and, consequently, for sites characterized by a σ bond with CO, in a higher stretching frequency of the carbonyl species. In our case, it is reasonable to hypothesize that the band at 2196 cm^{-1} reflects the presence of Ca^{2+} ions with a marked coordinative unsaturation formed by the added Cu centers, in agreement with the surface reconstruction hypothesis above proposed for the low concentrated Cu-samples.

The Cu3/HAP_D and Cu6/HAP_D catalysts were further comparatively characterized by HRTEM to investigate the morphological and structural properties of the samples depending on the Cu amount. The results of the characterization performed on Cu3/HAP_D and Cu6/HAP_D are shown in Fig. 6 and Fig. 7, respectively. The Cu3/HAP_D catalyst appears composed by large particles mainly with elongate shape alternated to globular ones (Fig. 6, panels a and b). Many regions of the sample are crystalline, as confirmed by the diffraction fringes with spacing related to crystalline HAP, according to the corresponding Fourier Transform (FT) of the images shown in Fig. 6 and in agreement with XRPD results. In addition, highly dispersed nanoparticles, appearing with poor contrast with respect to the HAP framework, were observed as can be appreciated in panel b of Fig. 6. The EDS analysis confirmed the presence of copper with relative amount corresponding to 2.36 ± 0.19 wt.% in the region where the nanoparticles can be clearly observed (Fig. 6, panel c). Moreover, the diffraction spots measured on the FT of the HRTEM images reveal that the spots connected to the copper-containing nanoparticles are possibly related to the (011), (120), (210), (220), (130), (310) and (131) planes of the orthorhombic libethenite phase ($Cu_2(PO_4)$ (OH) copper phosphate

hydroxide) observed previously in the XRPD pattern of the Cu9/HAP_D catalyst (Fig. 2, panel a). Libethenite nanoparticles have mean diameter d_m= 1.5 ± 0.5 nm (Fig. 6, panel d) and according to the particle size distribution, the large fraction of the nanoparticles has size between 1 and 2 nm.

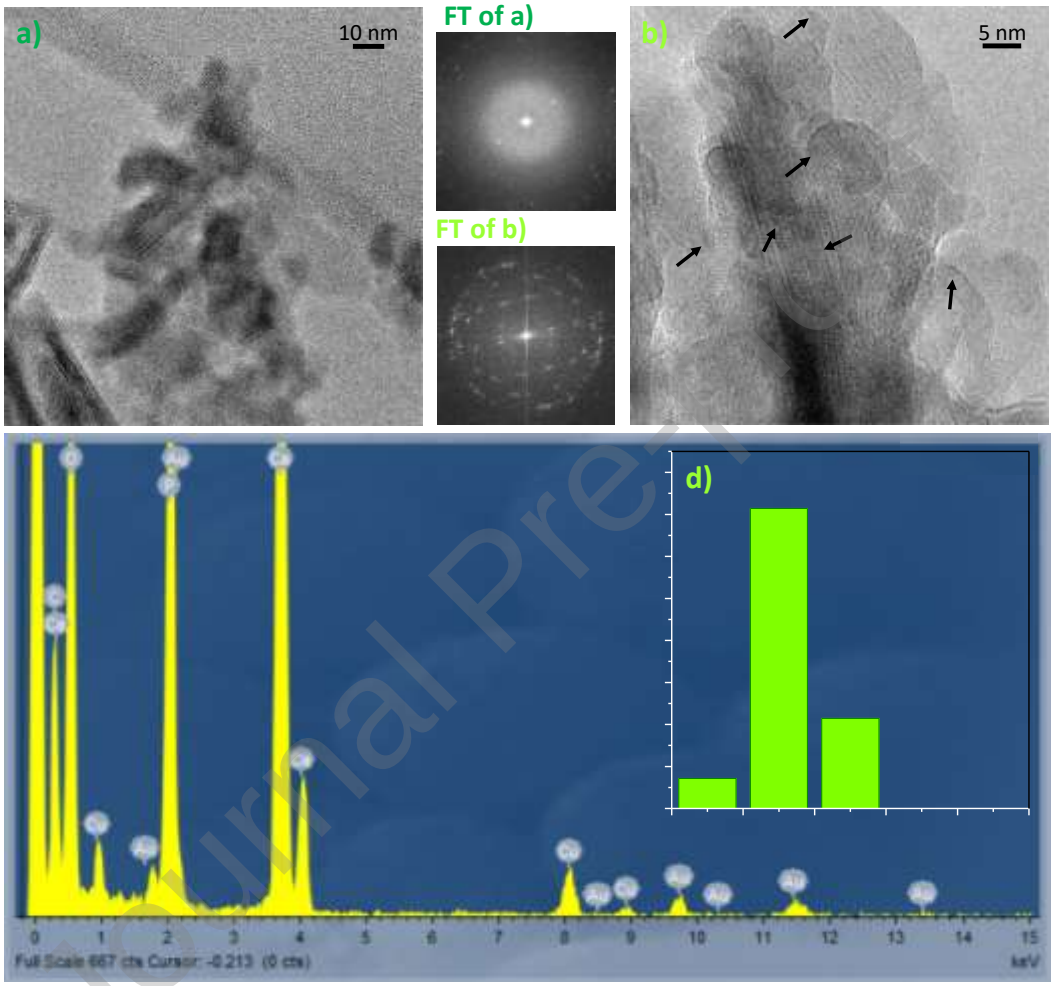

Figure 6. Representative HRTEM images of the Cu3/HAP_D catalyst (a and b). The presence of copper-containing nanoparticles is highlighted by harrows. EDS spectrum collected on the region shown in panel b (c) and particle size distribution (d). n.p. [%] = number of counted particles of diameter d_i. Instrumental magnification: 150000× (a) and 400000× (b).

Overall, both morphology and structure of the Cu6/HAP_D catalyst are the same as those observed in the case of Cu3/HAP_D, but the libethenite nanoparticles are more abundant than on the Cu3/HAP_D catalyst and can be observed already at lower magnification (in Fig. 7, the presence of libethenite nanoparticles is highlighted by harrows, panel a, 150000× and panel b, 400000×).

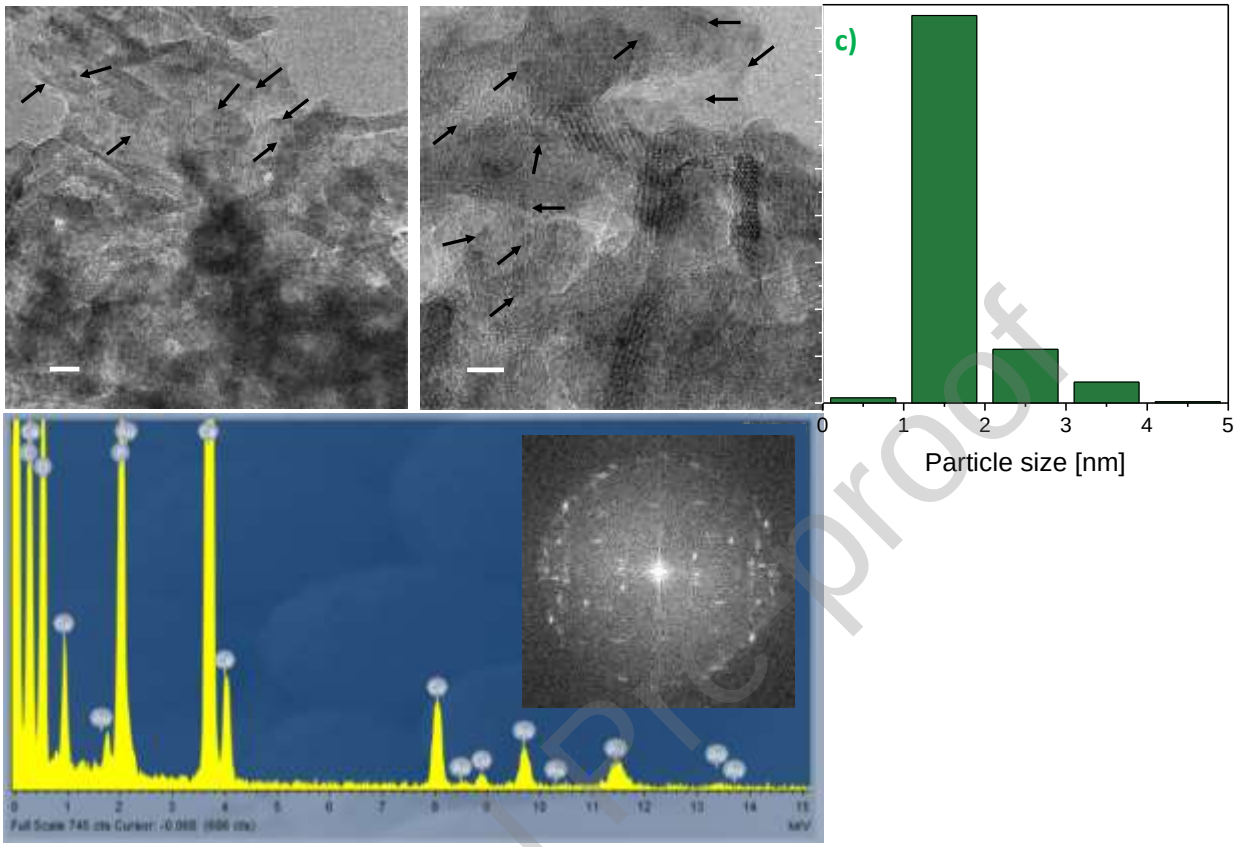

Figure 7. Representative TEM (a) and HR-TEM (b) images of the Cu6/HAP$_D$ catalyst. The presence of copper-containing nanoparticles is highlighted by harrows. Copper-containing particle size distribution (panel c). n.p. [%] = number of counted particles of diameter d_i. EDS spectrum of the region shown in panel b (d) and Fourier Transform of the HR-TEM image reported in panel b (inset). Instrumental magnification: 150000× (a) and 400000× (b).

In addition despite the higher Cu loading, the libethenite nanoparticles have quite similar average diameter d_m= 1.6 ± 0.6 nm (panel c of the same Figure). These findings are in agreement with the results of the EDS analysis, which confirm the higher relative amount of copper present in this sample (5.85 ± 0.27 wt. %, Fig. 7 panel d). Nevertheless, such nanoparticles appear homogeneously dispersed and arranged within the HAP matrix. The different abundance of libethenite nanoparticles depends on the Cu amount and could explain the lower availability of Cu cations on the Cu6/HAP$_D$

surface than on Cu3/HAP_D one put in evidence by FTIR, according to the different surface composition detected by XPS.

Summarizing the results obtained from the characterization studies, in particular CO absorption FTIR and HRTEM images, on the Cu/HAP_D and Fe/HAP_D samples, it is possible to rationalize the catalytic activity in the N_2O decomposition of Fig. 1. Concerning copper, on the HAP surface are found dispersed Cu nanoparticles, which prevail on Cu3/HAP_D, libethenite nanoparticles, which abound on Cu6/HAP_D, and libethenite phase, which predominates on Cu9/HAP_D. It emerges that a moderate structuring of copper particles is the winning key for an active catalyst of N_2O decomposition. The lowest catalytic activity of Cu9/HAP_D (Fig. 1) is due to the poor presence of Cu nanoparticles and the main presence of libethenite-structured copper at the surface. Concerning Fe, it emerges that a regular enrichment with isolated and dimeric iron centers occurred at the catalyst surfaces with increasing Fe-loading on HAP. Scheme 1 reports a comparative view of the Cu and Fe surfaces for Cu/HAP_D and Fe/HAP_D

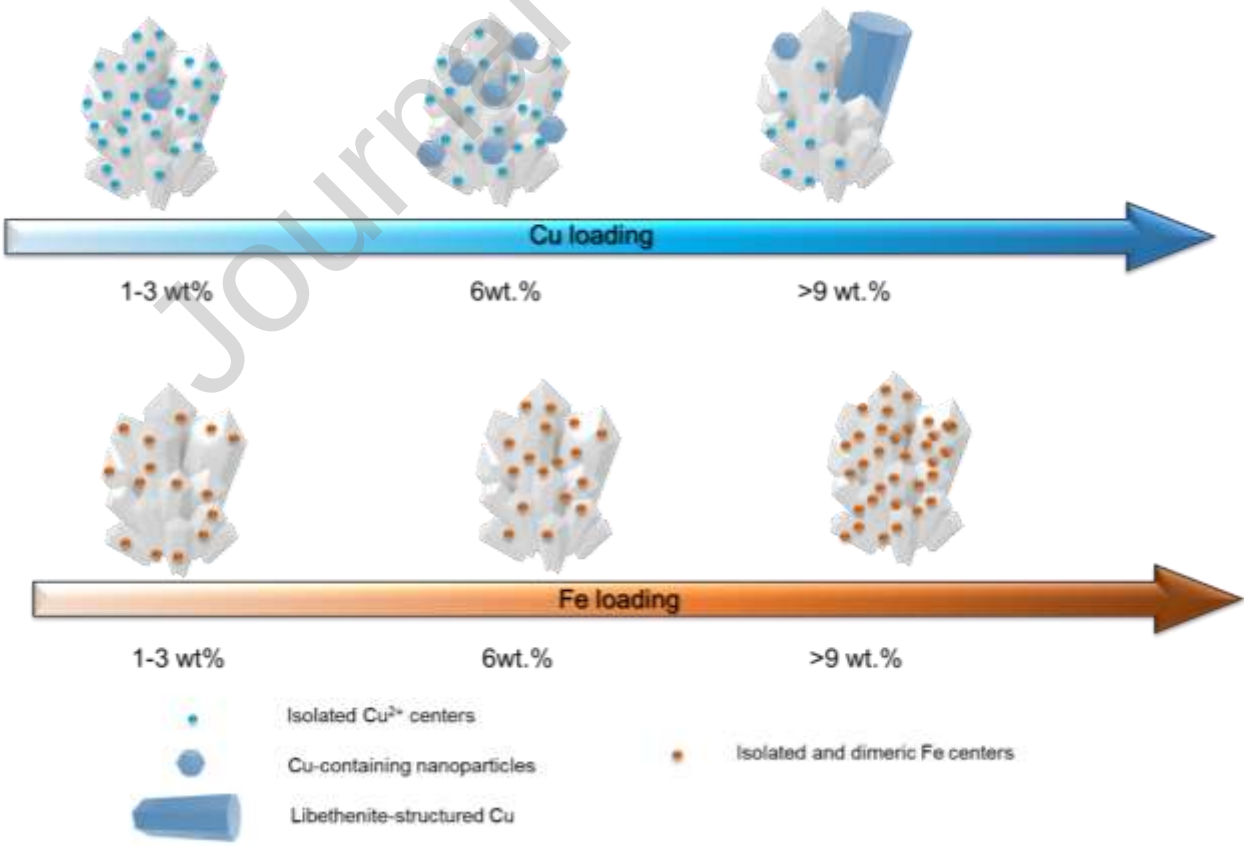

Scheme 1. Representation of Cu structuring trend on Cu/HAP_D (up) and Fe/HAP_D (bottom) catalysts at increasing Cu- and Fe-loading.

The emerged site heterogeneity of these catalysts makes the identification of the most active sites and related mechanism for N_2O decomposition not trivial. According to previous studies on copper- and iron-zeolite catalysts, dimeric Cu-O-Cu and Fe-O-Fe sites are recognized to be highly active in decomposing N_2O molecule [60]. Two different mechanisms, *single site* and *dual site* pathways, have been proposed, depending on N_2O coordination to the metal sites. The single-site route is characterized by higher activation barriers (150 kJ mol^{-1}) compared to dual site mechanism (80-100 kJ mol^{-1}) [60]. Starting from these premises, an insight on the active sites and mechanisms on our catalysts has been proposed based on additional kinetic elaboration. The apparent activation energies (E_{app}) and pre-exponential factors (A) were computed in the first-order kinetic hypothesis from the Arrhenius plot (Fig. S.5.) and the results are gathered in Table 2. In general, the obtained apparent activation energy values are lower than those typically reported for analogous Cu- and Fe-based zeolite catalysts. This could be due to the co-presence of Ca ions of hydroxyapatite structure, which could act as promoters. Actually, it has been reported that the addition of Ca ions to Co_3O_4 catalysts produces a significant enhancement in the catalytic performances in N_2O decomposition reaction with decreasing in the activation parameters [61].

The calculated E_{app} for Cu6/HAP_D are slightly higher than those for Fe9/HAP_D (49 vs. 35 kJ mol^{-1}), despite the higher N_2O conversion rates of Cu catalyst within the considered temperature window. This can be explained considering the much higher A value for Cu6/HAP_D, which also suggests a different transition state structure for N_2O decomposition. In any case, the low apparent activation energies suggest that the reaction likely occurs according to a *dual-site* mechanisms on the metal dimeric sites (Scheme 2). This hypothesis might also justify the higher activity of Cu6/HAP_D compared to Cu3/HAP_D and C9/HAP_D. Indeed, the chance for Cu-sites to locate close to each other to form dimeric pairs is high on small Cu nanoparticles, which are the prevalent Cu species in Cu6/HAP_D.

Table 2. Kinetic Results for the Decomposition of N_2O on hydroxyapatite-based catalysts

Catalyst	Initial rate [a] ($\mu mol_{N2O}\ g_{cat}^{-1}\ min^{-1}$)	E_{app} (kJ mol^{-1})	ln A	R^2
$Cu6/HAP_D$	0.39	49.11 ± 1.01	8.53 ± 0.19	0.999
$Fe9/HAP_D$	0.32	34.80 ± 3.49	5.60 ± 0.62	0.961
HAP	0.12	21.27 ± 0.69	2.57 ± 0.50	0.943

[a] Calculated for a reaction temperature of 350°C

The proposed *dual site* mechanism for the N_2O decomposition involves an initial N_2O chemisorption step followed by dissociation into nitrogen and chemisorbed oxygen. The latter can then migrate and combine to O_2 according to a Langmuir-Hinshelwood mechanism [62]. Two are the main requirements for high activity in this process: i) strong interaction between N_2O molecule and the metal site to promote dissociation and ii) formation of labile surface oxygen to finalize the catalytic cycle by O_2 desorption. Consequently, the better performance of Cu/HAP catalysts compared to iron-based ones might essentially derive from strong bond interaction between N_2O and Cu sites. Actually, microcalorimetric and spectroscopic studies reported by Rakić et al. [63] demonstrated that N_2O establishes significantly stronger interactions with Cu-ZSM-5 than with Co- or Fe-ZSM-5. Another advantage of copper over iron is its superior redox ability which facilitates chemisorbed O mobility and desorption as O_2.

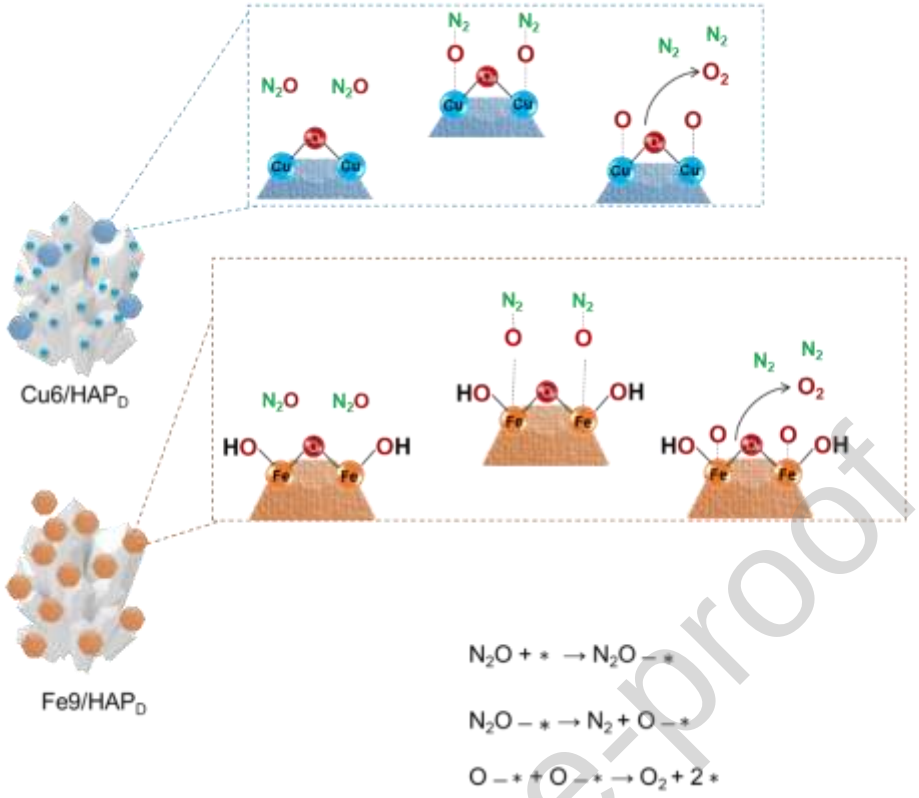

Scheme 2. Dual-site reaction mechanism over Cu- and Fe-containing catalysts (the dotted black segments connecting O-atoms of N_2O molecules to metal sites symbolize the coordination bonds, their length is inversely proportional to the interaction strength, i.e. the longer the segment, the weaker the interaction; ∗ represents an active site of the catalyst)

3.4 Reusability tests and time-on-stream stability

The reusability of Cu6/HAP$_D$ and Fe9/HAP$_D$ catalysts was tested in four subsequent runs of N_2O decomposition performed by using for each run the catalyst recovered after the previous one.

In both catalysts, a general decrease in the activity was observed between the first and the second run. This appeared clear from the 2nd run curves in Fig. 8 that resulted to be shifted at higher temperature values compared to those of the 1st run. The shift was significantly more pronounced in the case of iron-containing catalyst, likely due to the fact that in this case the superior limit of the operating temperature window (650°C) was higher than the calcination temperature (650°C). Anyway, a stabilization of the catalysts was more or less evident after the second run.

The used samples after 4 runs had a similar surface composition, as determined by XPS, to that of the samples before reaction, without any remarkable difference in the (Me+Ca)/P ratios (Table S.3., Fig. S.6.). XRPD of the used Cu6/HAP_D and Fe9/HAP_D after 4 runs showed additional crystalline phases, besides HAP, ascribable to calcium copper phosphate and calcium iron phosphate (see discussion here below reported). The surface reconstruction could be likely due to the long-term exposure of the catalysts at high temperatures.

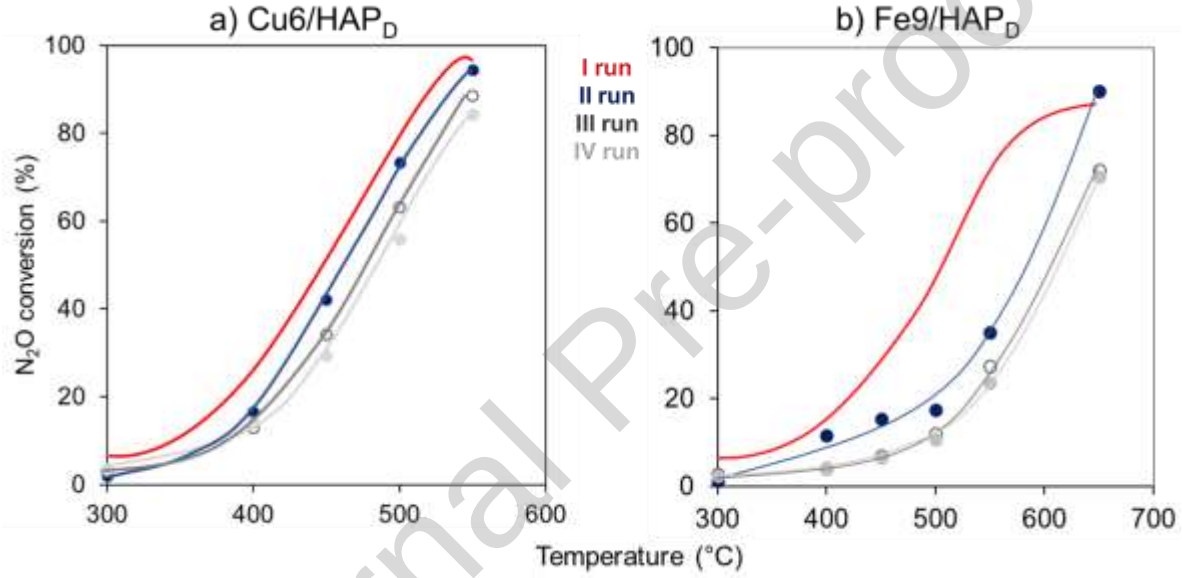

Figure 8. Reusability tests (I-IV runs) over Cu6/HAP_D and Fe9/HAP_D samples (a and b panels, respectively): profiles of N_2O conversion (%) as a function of temperature (°C).
Reaction conditions for each run: [N_2O] =150 ppm, [O_2]= 6,000 ppm, contact time= 0.12 s.

To further study the long-term stability of the catalysts under reaction conditions, the time-on-stream stability of Cu6/HAP_D and Fe9/HAP_D was evaluated at 550°C by keeping all the other parameters constant. As shown in Fig. 9, except a slight decrease in N_2O conversion within the first 10 h, the catalysts sustained very high activity (ca. 80% and 55% N_2O conversion for Cu- and Fe-based catalysts, respectively) over 72 h. The initial deactivation observed is probably due to stress of the catalyst which was maintained at a temperature of 550°C for a longer time than the duration of calcination.

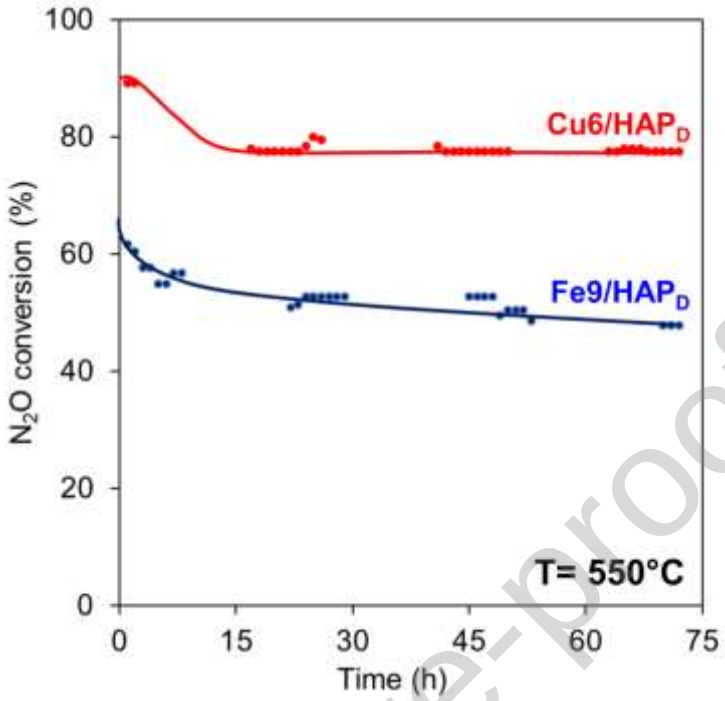

Figure 9. Time-on-stream stability tests at fixed temperature (550°C): profiles of N_2O conversion (%) along with time (h) over Cu6/HAP_D (red) and Fe9/HAP_D (blue).
Reaction conditions: [N_2O] =150 ppm, [O_2] =6,000 ppm, contact time= 0.12 s.

3.5 De-N_2O activity in the presence of poisons

Besides activity, selectivity, and stability, an efficient catalyst must be tolerant to various poisons that could be co-fed with the main reagent species. Sulphur in fuel and engine lubricating oil can be present in a non-negligible quantity, then, exhaust gases may contain SO_2 besides the NO_x pollutants that must be abated. Unfortunately, SO_2 is reported to poison several active de-NOx catalysts (e.g., metal loaded zeolites) and the search for sulphur-tolerant catalysts is an important challenge [64,65].

The sulphur tolerance of the Cu6/HAP_D and Fe9/HAP_D samples was explored during de-N_2O reaction, continuously feeding a reaction gaseous mixture containing SO_2 (*ca*. 50 ppm of SO_2 with 150 ppm of N_2O, and 6,000 ppm of O_2) while the temperature was increased from 300° to 700°C.

A comparison of the N_2O conversion profiles as a function of temperature obtained in the absence/presence of SO_2 is showed in Fig. 10. On Cu6/HAP_D, the two conversion-temperature profiles with/without presence of SO_2 are similar but the curve collected in the SO_2 presence shifted at an increasing temperature of *ca*. 100°C at any N_2O conversion value (Fig. 10, panel a). Then, a maximum conversion of 97% of the N_2O fed was achieved at the temperature of 650°C, higher than that observed in the absence of SO_2 (550° C). A different behaviour was observed on Fe9/HAP_D (Fig. 10 panel b); N_2O conversion in the SO_2 presence quite overlapped the curve collected without SO_2 up to ca. 40% conversion (500°C), then it deviated and always remained below that collected in the absence of SO_2. Nevertheless, 97% N_2O conversion was achieved at the temperature of 750°C.

Results obtained on the two Cu- and Fe-catalysts indicate that both the catalysts seem to be tolerant to SO_2 in the whole studied temperature range. The conversion-temperature profiles indicate that the more active Cu- and Fe-sites, likely those at interstitial/defectual positions, could be irreversibly poisoned by SO_2, but most of the metal sites can maintain activity towards N_2O decomposition even in the SO_2 presence. The formation of copper sulphate or iron sulphate should be responsible for the metal sites poisoning, as reported in several studies [66,67]; the curves of Fig. 10 showed that a higher temperature was needed to poison Fe sites than the Cu sites.

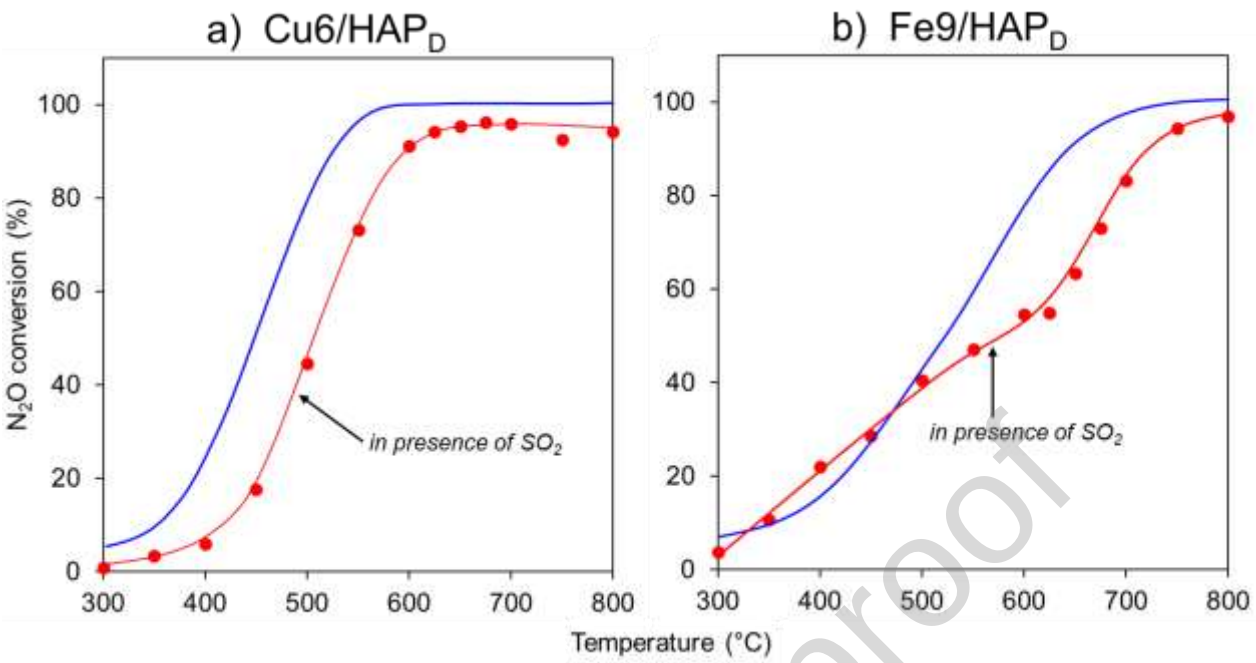

Figure 10. De-N_2O catalytic activity results over Cu6/HAP_D and Fe9/HAP_D (a and b panels, respectively) performed in presence of SO_2 in the gaseous stream (red lines) compared with profiles reported in Fig.1. Reaction conditions: [N_2O] =150 ppm, [O_2] =6,000 ppm, [SO_2]=50 ppm, contact time= 0.12 s.

In addition, it is interesting to note that during the catalytic tests, SO_2 concentration (continuously monitored by FTIR by the line at 1360.4 cm^{-1}) exponentially decreased when the reaction mixture contacted the catalysts and it remained to zero up to the end of the reaction test. Probably, the adsorption of SO_2 occurred on the basic sites of the HAP-support surface which, with a sort of sacrificial mechanism, allowed most of the metal sites to remain free and active for the decomposition of N_2O. The use of HAP as support for Cu- and Fe-sites could be a winning choice due to the amphoteric feature of this material, which possesses both acid and base sites at its surface [68]. The base sites of HAP are of high basic strength and could react with acidic species, i.e. SO_2, present in the gaseous reaction mixture.

The presence of SO_2 on the surfaces of the catalyst was demonstrated by XPS analysis. Samples Cu6/HAP_D and Fe9/HAP_D and also bare HAP, after being used in the N_2O decomposition test up to 600°C were analyzed by XPS. On these samples, the analyses revealed an amount of sulphur not

dissimilar between HAP and metal loaded HAP samples (Table S.4.). Furthermore, the HR spectrum of the S 2p region (160-180 eV, Figure S.7.) revealed several species associated with the presence of sulphur, which was present in the form of sulphur dioxide (167 eV), sulphites (168.5 eV) and sulphates (170 -171 eV), without the possibility of distinguishing different contributions in quantity and nature of the sulphur formed on the surfaces between HAP and metal-containing HAP.

Also, some alkali species can be present in the exhaust gases containing N_2O to be decomposed so limiting the activity of catalysts if they are not alkali-tolerant.

To verify the alkali tolerance properties of our metal loaded HAP samples, Cu6/HAP_D and Fe9/HAP_D were doped with certain amount of K and Ba, to simulate an alkali poisoning covering some parts of the catalyst surfaces, probably blocking some active sites as well. The as-obtained samples (labelled as Cu6/$HAP_{D,K}$, Cu6/$HAP_{D,Ba}$, and Fe9/$HAP_{D,K}$, Fe9/$HAP_{D,Ba}$) possessed a 1:10 molar ratio between alkali species and metal species. The two Cu-samples had *ca*. 0.22 wt.% and 0.91 wt.% of K and Ba, respectively, and Fe-samples had 0.32 wt.% and 1.48 wt.% of K and Ba, respectively. The obtained K- and Ba-loadings indicate that Ba^{2+} was more effectively adsorbed than K^+ on HAP, in agreement with the known capacity of HAP to exchange Ca^{2+} cations with bivalent metal cations.

Both the poisoned alkali-samples were tested in the N_2O-decomposition reaction; Fig. 11 reports the collected N_2O conversion-temperature profiles. As for the test in the presence of SO_2, the results showed that for Cu6/$HAP_{D,K}$ and Cu6/$HAP_{D,Ba}$ only a slight decrease in activity was observed, shifted to slightly higher temperatures than in sample without alkali. As for the two alkali poisoned Fe catalysts, Ba-poisoning caused a decrease in N_2O activity, conversion-temperature curve shifted to higher temperatures, with the attainment of 100% N_2O conversion at 800°C, whereas a different behaviour was detected in the case of the K-poisoning sample. In this latter case, the activity shifted to higher temperature, as in the case of Ba-poisoned sample, but starting from *ca*. 650°C, N_2O conversion drastically dropped down to *ca*. 50% at the maximum attained temperature. XRPD analysis of the used alkali-poisoned samples after the catalytic test of N_2O decomposition (Fig. 11)

showed the formation of additional crystalline phases besides HAP, that were not present on the fresh catalysts (i.e., potassium calcium iron phosphate, JCPDS 00-053-0777). The other newly formed phases (likely, calcium copper phosphate and calcium iron phosphate) in the poisoned Cu and Fe catalysts probably result from the high temperatures used in the N_2O decomposition test; their formation did not negatively affect the catalytic performances.

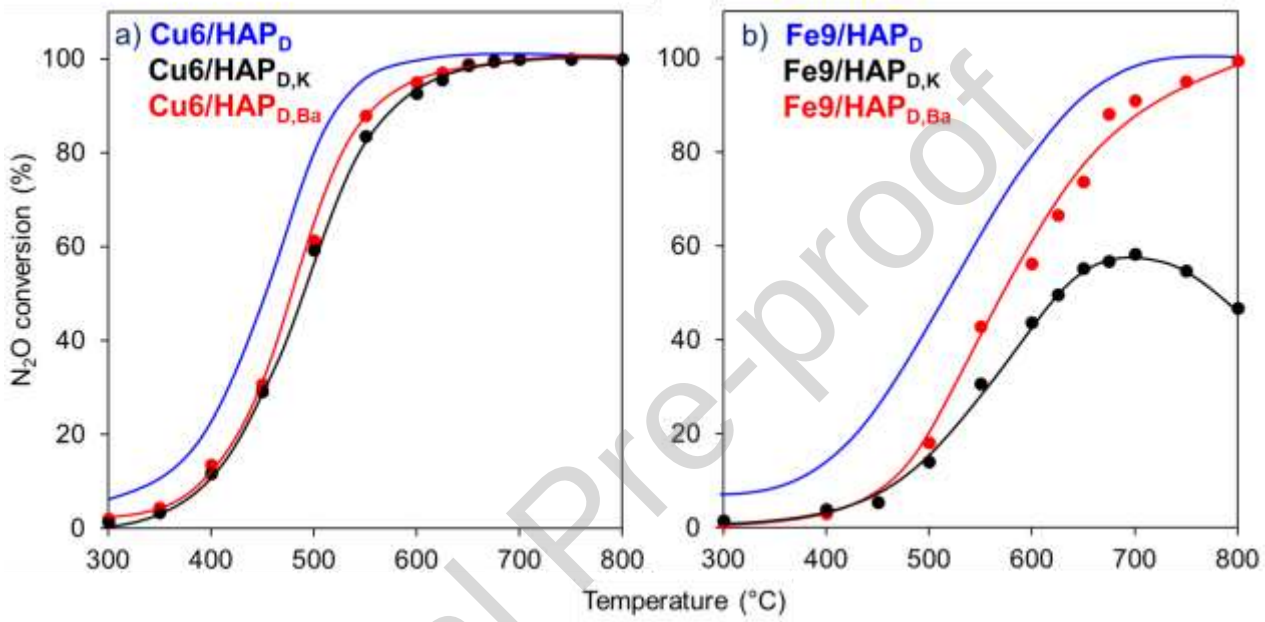

Figure 11. De-N_2O catalytic activity results over Cu6/$HAP_{D,K/Ba}$ and Fe9/$HAP_{D,K/Ba}$ samples (a and b panels, respectively) doped with Ba- and K-species (red and black lines, respectively) compared with profiles reported in Fig. 1. Reaction conditions: [N_2O] =150 ppm, [O_2] =6,000 ppm, contact time= 0.12 s.

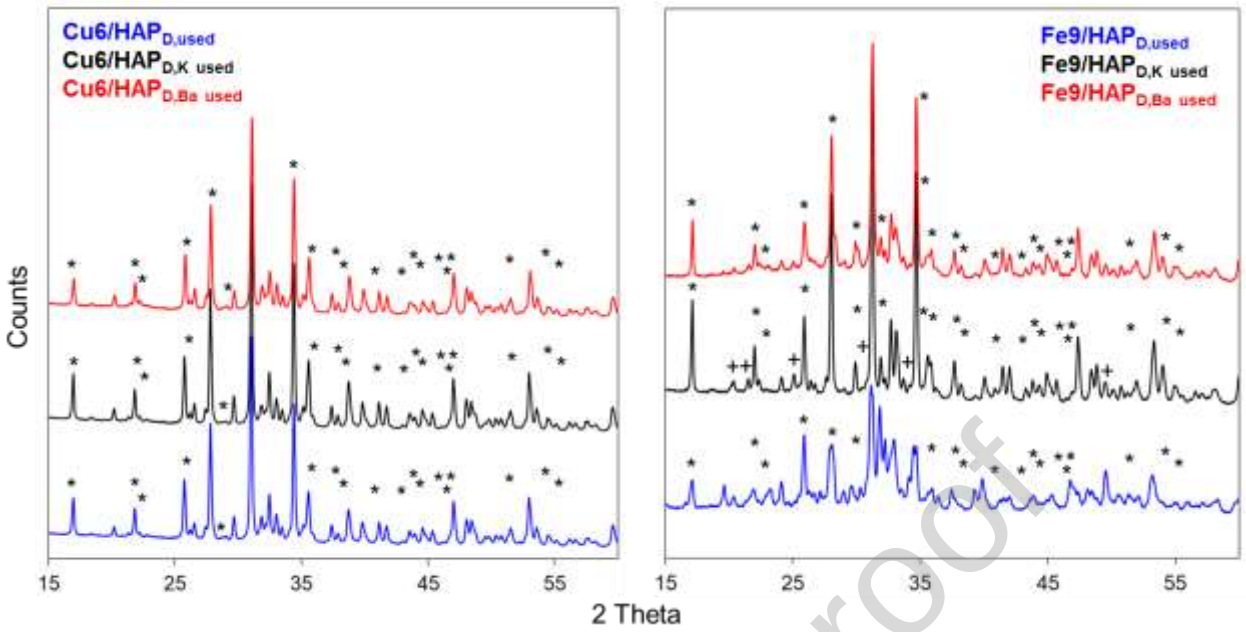

Figure 12. XRPD patterns of used Cu6/HAP_D, Fe9/HAP_D and of samples poisoned with K- and Ba-species after de-N_2O catalytic tests with the related identified references (*: calcium copper phosphate and calcium iron phosphate, left and right panels; +: potassium calcium iron phosphate, JCPDS 00-053-0777 right panel).

4. Conclusions

From the present study, it emerges that new effective catalysts based on metal-functionalized hydroxyapatite material with biocompatible and sustainable properties can be taken into consideration for the direct catalytic decomposition of N_2O, a difficult reaction requiring high temperature for activation.

An optimized content of copper or iron could impart good activity to hydroxyapatite. The activities of Fe- and Cu-based catalysts for N_2O decomposition were quite different. Cu-containing catalysts were active in a lower temperature range than Fe-based ones.

The metal distribution on the hydroxyapatite surface depended on metal loading and nature that govern the structuration and surfacing of the metal phases with consequences on catalytic activities.

As for Cu-catalysts, a moderate structuration with nanoparticles size around 1.6 nm gives rise to highly active and selective catalyst. Differently for Fe-catalysts, from 3 up to 9% of iron loading, an

increasing gradual trend in activity can be noted. This seems to be connected with a gradual coverage of HAP surface by isolated and dimeric Fe-species. These results evidence the key role of the nature and nucleation of metal species generated over the catalyst surfaces.

From an application point of view, Cu- and Fe-functionalized hydroxyapatites demonstrated to be promising de-N_2O catalysts since they display good long-term stability and remarkable sulfur resistance and tolerance to alkali-poisoning. In a future investigation, the catalyst emerged as the most promising (i.e., Cu6/HAP_D) will be studied in a defined atmosphere, paying attention to the co-presence of water or other species which are typically present in N_2O containing emissions.

Acknowledgements

Solvay, Soda Ash and Derivatives, Rue de Ransbeek 310, Bruxelles, is gratefully acknowledged for supplying hydroxyapatite.

The use of instrumentation purchased through the SmartMatLab Project of Dipartimento di Chimica (Cariplo Foundation, project 2013-1776) is gratefully acknowledged and also Dr. Daniele Marinotto of Consiglio Nazionale delle Ricerche (CNR), Istituto di Scienze e Tecnologie Molecolari (ISTM).

References

[1] A. Fihri, C. Len, R.S. Varma, A. Solhy, Coord Chem Rev 347 (2017) 48–76.

[2] M. Ibrahim, M. Labaki, J.-M. Giraudon, J.-F. Lamonier, J Hazard Mater 383 (2020) 121139.

[3] S. Campisi, C. Castellano, A. Gervasini, New Journal of Chemistry 42 (2018) 4520–4530.

[4] S. Campisi, C. Evangelisti, G. Postole, A. Gervasini, Appl Surf Sci 539 (2021) 148227.

[5] Y. Chen, S. Shu, S. Wang, J. Li, Journal of Inorganic Materials 37 (2022) 1065.

[6] M.G. Galloni, S. Campisi, S.G. Marchetti, A. Gervasini, Catalysts 10 (2020) 1415.

[7] S. Campisi, M.G. Galloni, S.G. Marchetti, A. Auroux, G. Postole, A. Gervasini, ChemCatChem 12 (2020) 1676–1690.

[8] S. Campisi, M.G. Galloni, F. Bossola, A. Gervasini, Catal Commun 123 (2019) 79–85.

[9] M. Schiavoni, S. Campisi, P. Carniti, A. Gervasini, T. Delplanche, Appl Catal A Gen 563 (2018) 43–53.

[10] L. Li, J. Xu, J. Hu, J. Han, Environ Sci Technol 48 (2014) 5290–5297.

[11] E.A. Davidson, D. Kanter, Environmental Research Letters 9 (2014).

[12] R.K. Pachauri, A. Reisinger, L. Bernstein, Intergovernmental Panel on Climate Change. Core Writing Team, Intergovernmental Panel on Climate Change, Climate Change 2007 : Synthesis Report, n.d.

[13] United Nations Environment Programme, Drawing down N_2O to Protect Climate and the Ozone Layer : A UNEP Synthesis Report, 2013.

[14] J. Pérez-Ramírez, F. Kapteijn, K. Schöffel, J.A. Moulijn, Appl Catal B 44 (2003) 117–151.

[15] T. Selleri, R. Gioria, A.D. Melas, B. Giechaskiel, F. Forloni, P. Mendoza Villafuerte, J. Demuynck, D. Bosteels, T. Wilkes, O. Simons, P. Recker, V. Lilova, Y. Onishi, M. Steffen, B. Grob, A. Perujo, R. Suarez-Bertoa, Catalysts 12 (2022) 184.

[16] F. Kapteijn, J. Rodriguez-Mirasol, J.A. Moulijn, Appl Catal B 9 (1996) 25–64.

[17] G. Centi, F. Vazzana, Catal Today 53 (1999) 683–693.

[18] K.M. Nicholas, C. Lander, Y. Shao, Inorg Chem 61 (2022) 14591–14605.

[19] M. Jabłońska, R. Palkovits, Catal Sci Technol 6 (2016) 7671–7687.

[20] N. Richards, J.H. Carter, E. Nowicka, L.A. Parker, S. Pattisson, Q. He, N.F. Dummer, S. Golunski, G.J. Hutchings, Appl Catal B 264 (2020) 118501.

[21] G. Centi, L. Dall'olio, S. Perathoner, Catal Letters 67 (2000) 107–112.

[22] G.E. Marnellos, E.A. Efthimiadis, I.A. Vasalos, Appl Catal B 46 (2003) 523–539.

[23] G. Centi, A. Galli, B. Montanari, S. Perathoner, A. Vaccaria, Catal Today 35 (1997) 113–120.

[24] M. Konsolakis, ACS Catal 5 (2015) 6397–6421.

[25] M. Jabłońska, R. Palkovits, Catal Sci Technol 6 (2016) 49–72.

[26] S. Bennici, A. Gervasini, Appl Catal B 62 (2006) 336–344.

[27] F. Lin, T. Andana, Y. Wu, J. Szanyi, Y. Wang, F. Gao, J Catal 401 (2021) 70–80.

[28] J. Pérez-Ramírez, F. Kapteijn, G. Mul, J.A. Moulijn, Appl Catal B 35 (2002) 227–234.

[29] A. Wang, Y. Wang, E.D. Walter, R.K. Kukkadapu, Y. Guo, G. Lu, R.S. Weber, Y. Wang, C.H.F. Peden, F. Gao, J Catal 358 (2018) 199–210.

[30] T. Nobukawa, M. Yoshida, K. Okumura, K. Tomishige, K. Kunimori, J Catal 229 (2005) 374–388.

[31] A. Heyden, B. Peters, A.T. Bell, F.J. Keil, Journal of Physical Chemistry B 109 (2005) 1857–1873.

[32] A. Heyden, N. Hansen, A.T. Bell, F.J. Keil, Journal of Physical Chemistry B 110 (2006) 17096–17114.

[33] G. Sádovská, E. Tabor, P. Sazama, M. Lhotka, M. Bernauer, Z. Sobalík, Catal Commun 89 (2017) 133–137.

[34] Y. Li, J.N. Armor, Appl Catal B 1 (1992) L21–L29.

[35] C. Chen, Y. Cao, S. Liu, W. Jia, Appl Surf Sci 507 (2020) 145153.

[36] G.E. Marnellos, E.A. Efthimiadis, I.A. Vasalos, Appl Catal B 46 (2003) 523–539.

[37] X. Wei, Y. Wang, X. Li, R. Wu, Y. Zhao, Molecular Catalysis 491 (2020) 111005.

[38] C. Huang, Z. Ma, P. Xie, Y. Yue, W. Hua, Z. Gao, J Mol Catal A Chem 400 (2015) 90–94.

[39] L. Zoubeir, S. Adeline, C.S. Laurent, C. Yoann, H.T. Truc, L.G. Benoît, A. Federico, J Hazard Mater 148 (2007) 606–612.

[40] M.D. Mann, M.E. Collings, P.E. Botros, Prog Energy Combust Sci 18 (1992) 447–461.

[41] P. Perrin, O.J.F.J.G.; Bodson, T. Delplanche, D. Breugelmans, Process for Producing a Calcium Phosphate Reactant, Reactant Obtained and Use Thereof in the Purification of Liquid Effluents, WO 2015/173437 Al, 2015.

[42] A. Gervasini, C. Messi, P. Carniti, A. Ponti, N. Ravasio, F. Zaccheria, J Catal 262 (2009) 224–234.

[43] A. Gervasini, M. Marzo, Adsorption Science & Technology 29 (2011) 365–379.

[44] Z. Boukha, M. Kacimi, M.F.R. Pereira, J.L. Faria, J.L. Figueiredo, M. Ziyad, Appl Catal A Gen 317 (2007) 299–309.

[45] Y. Li, C. TeckNam, C. PingOoi, J Phys Conf Ser 187 (2009).

[46] D. Chlala, M. Labaki, J.-M. Giraudon, O. Gardoll, A. Denicourt-Nowicki, A. Roucoux, J.-F. Lamonier, Comptes Rendus Chimie 19 (2016) 525–537.

[47] H. Tounsi, S. Djemal, C. Petitto, G. Delahay, Appl Catal B 107 (2011) 158–163.

[48] P.A. Kumar, M.P. Reddy, L.K. Ju, H.H. Phil, Catal Letters 126 (2008) 78–83.

[49] D. Chlala, A. Griboval-Constant, N. Nuns, J.M. Giraudon, M. Labaki, J.F. Lamonier, Catal Today 307 (2018) 41–47.

[50] Y. Wang, B. Chen, M. Crocker, Y. Zhang, X. Zhu, C. Shi, Catal Commun 59 (2015) 195–200.

[51] M. Khachani, M. Kacimi, A. Ensuque, J.Y. Piquemal, C. Connan, F. Bozon-Verduraz, M. Ziyad, Appl Catal A Gen 388 (2010) 113–123.

[52] Z. Boukha, M. Kacimi, M. Ziyad, A. Ensuque, F. Bozon-Verduraz, J Mol Catal A Chem 270 (2007) 205–213.

[53] M.S. Kumar, M. Schwidder, W. Grünert, A. Brückner, J Catal 227 (2004) 384–397.

[54] G. Centi, S. Perathoner, F. Pino, R. Arrigo, G. Giordano, A. Katovic, V. Pedulà, Catal Today 110 (2005) 211–220.

[55] R.P. Vasquez, Surface Science Spectra 5 (1998) 273–278.

[56] C. Morterra, V. Bolis, G. Magnacca, G. Cerrato, J Electron Spectros Relat Phenomena 64–65 (1993) 235–240.

[57] P. Hollins, J. Pritchard, Surf Sci 89 (1979) 486–495.

[58] K.I. Hadjiivanov, G.N. Vayssilov, in: Advances in Catalysis, Academic Press, 2002, pp. 307–511.

[59] V. Bolis, B. Fubini, E. Garrone, E. Giamello, C. Morterra, in: C. Morterra, A. Zecchina, G. Costa (Eds.), Structure and Reactivity of Surfaces, 1989, pp. 159–166.

[60] F. Lin, T. Andana, Y. Wu, J. Szanyi, Y. Wang, F. Gao, J Catal 401 (2021) 70–80.

[61] Q. Zhang, X. Tang, P. Ning, Y. Duan, Z. Song, Y. Shi, RSC Adv 5 (2015) 51263–51270.

[62] A. Wang, Y. Wang, E.D. Walter, R.K. Kukkadapu, Y. Guo, G. Lu, R.S. Weber, Y. Wang, C.H.F. Peden, F. Gao, J Catal 358 (2018) 199–210.

[63] V. Rakić, V. Rac, V. Dondur, A. Auroux, in: Catal Today, Elsevier, 2005, pp. 272–280.

[64] L. Zhao, Y. Zhang, M. Kang, Environmental Engineering Research 27 (2021) 200642–0.

[65] A.Yu. Molokova, E. Borfecchia, A. Martini, I.A. Pankin, C. Atzori, O. Mathon, S. Bordiga, F. Wen, P.N.R. Vennestrøm, G. Berlier, T.V.W. Janssens, K.A. Lomachenko, JACS Au 2 (2022) 787–792.

[66] G. Yang, X. Du, J. Ran, X. Wang, Y. Chen, L. Zhang, The Journal of Physical Chemistry C 122 (2018) 21468–21477.

[67] W. Su, Z. Li, Y. Zhang, C. Meng, J. Li, Catal. Sci. Technol. 7 (2017) 1523–1528.

[68] L. Silvester, J.-F. Lamonier, R.-N. Vannier, C. Lamonier, M. Capron, A.-S. Mamede, F. Pourpoint, A. Gervasini, F. Dumeignil, J. Mater. Chem. A 2 (2014) 11073–11090.

[69] G. He, B. Zhang, H. He, X. Chen, Y. Shan, Science of the Total Environment 673 (2019) 266–271.

[70] J. bin Lim, S.H. Cha, S.B. Hong, Appl Catal B 243 (2019) 750–759.

[71] P. Xie, Z. Ma, H. Zhou, C. Huang, Y. Yue, W. Shen, H. Xu, W. Hua, Z. Gao, Microporous and Mesoporous Materials 191 (2014) 112–117.

AUTHOR CONTRIBUTIONS

M.G. Galloni: Investigation, Formal analysis, Writing - Original Draft. **S. Campisi:** Conceptualization, Methodology, Formal analysis, Writing - Review & Editing, Visualization. **A. Gervasini:** Conceptualization, Methodology, Writing - Review & Editing, Supervision. **S. Morandi:** Investigation, Writing - Original Draft. **M. Manzoli:** Investigation, Writing - Original Draft.

Declaration of interests

☒ The authors declare that they have no known competing financial interests or personal relationships that could have appeared to influence the work reported in this paper.

☐The authors declare the following financial interests/personal relationships which may be considered as potential competing interests:

HIGHLIGHTS

- Efficient hydroxyapatite catalysts may be prepared from waste materials;
- Nitrous oxide is successfully decomposed on copper or iron hydroxyapatite catalysts
- Moderate copper structuring resulted the key factor for good activity
- Catalysts have long term stability, sulphur and alkali resistance